Effect of a resistive load on the starting performance of a standing wave thermoacoustic engine: a numerical study

Lin Ma, Catherine Weisman[a)], Diana Baltean-Carlès, Ivan Delbende

Université Pierre et Marie Curie UPMC Sorbonne Universités,

Laboratoire d'Informatique pour la Mécanique et les Sciences de l'Ingénieur Orsay,

France

and Luc Bauwens

Department of Mechanical and Manufacturing Engineering

University of Calgary

Canada

Onset of loaded thermoacoustic engine

[a)]e-mail: catherine.weisman@limsi.fr

Abstract

The influence of a resistive load on the starting performance of a standing-wave thermoacoustic engine is investigated numerically. The model used is based upon a low Mach number assumption; it couples the two-dimensional nonlinear flow and heat exchange within the thermoacoustic active cell with one-dimensional linear acoustics in the loaded resonator. For a given engine geometry, prescribed temperatures at the heat exchangers, prescribed mean pressure and prescribed load, results from a simulation in the time domain include the evolution of the acoustic pressure in the active cell. That signal is then analyzed, extracting growth rate and frequency of the dominant modes. For a given load, the temperature difference between the two sides is then varied; the most unstable mode is identified, and so is the corresponding critical temperature ratio between heater and cooler. Next, varying the load, a stability diagram is obtained, potentially with predictive value. Results are compared with those derived from Rott's linear theory as well as with experimental results found in the literature.

PACS numbers: 43.35.Ud

I. INTRODUCTION

A thermoacoustic engine is a device absorbing heat at the hot heat exchanger and releasing heat at the cold heat exchanger while producing acoustic work as an output. Engines are meant to carry a load, which in the case of an acoustic device, might include a thermoacoustic refrigerator[1], a pulse tube refrigerator[2], a (possibly linear) electric generator[3] or a piezoelectric transducer[4]. The strong coupling that will exist between the engine and the load influences both starting performance and steady (periodic) operation.

Thermoacoustic devices have been studied extensively for more than 30 years. Most of the work in the literature is based upon the linear theory, developed by Rott[5] and later extended by Swift et al.[1;6]. The theory can handle different geometries for the various parts of the system, such as, stack, heat exchangers, ducts. Numerical implementation is based upon a lumped element approximation[7]. The linear theory will then yield the acoustic field and as a result, the performance of a given system when in the periodic regime[1]. Linear theory can also predict the onset conditions (critical starting temperature gradient) as a function of the mean pressure, by performing a stability analysis for a fixed geometry and working fluid. Results from linear theory are in good agreement with experiments[8;9;10] for the onset of a standing wave thermoacoustic engine inside a resonator closed at both ends. Recently, a completely analytical boundary layer theory extending linear theory was developed by Sugimoto[11;12], reducing the problem to a one dimensional model. That theory was then used in an analytical stability analysis for systems with a stack under given temperature gradient inside straight or looped resonators, for given acoustic frequency, without resorting to lumped elements. Linear theory has important limitations: the stability analysis is performed in the frequency domain for each mode; the transient regime is not described; non linear and multidimensional effects are not considered or are only partially taken into account.

Transient regimes were addressed by de Waele[13], who developed a one-dimensional time-dependent model of a thermoacoustic Stirling engine taking into account the dynamics of individual components, again using a lumped-element approximation. De Waele studied engine start phase and transient effects while acoustics is still considered linear. A mixed empirical and theoretical one-dimensional model was developed by Guedra et. al[14;15], based upon a transmission matrix formulation, also assuming linear acoustics. The transmission matrix is obtained experimentally from impedance measurements. Using that model, they studied the onset of oscillations for both a basic standing wave engine and a traveling wave-engine. None of these studies included the influence of a load on onset conditions.

In contrast, the influence of the load has been accounted for in studies of thermoacoustic devices in the periodic regime. The performance of a loaded thermoacoustic engine was investigated by Olson et. al[16], and also others[17;18], using linear theory[1] and the lumped elements approximation. More recently, Hatori et al.[19] developed an experimental method based on measuring the acoustic impedance of the engine and of the load separately, and predicted the operating point of the combination engine plus load. Coming to nonlinear models, some numerical simulations of the full compressible Navier-Stokes equations in loaded thermoacoustic devices with complicated geometry have been performed[20;21]. These simulations were performed using commercial codes and gave good description of thermoacoustic engines in the transient and periodic regime. However each test case required extremely large and time consuming simulations; therefore these are not appropriate for a parametric study of a variable load coupled with an engine.

The aim of the current work is to study the influence of a variable load on the marginal stability conditions of a standing-wave thermoacoustic engine. The model used implements a hybrid low Mach number approximation. It is based on coupling the two-dimensional nonlinear flow and heat exchange in the thermoacoustic active cell with one-dimensional linear acoustics in the loaded resonator. For a detailed description see Ref.[22]. In the load model used in the present study, instantaneous acoustic pressure and velocity are assumed to be in phase at the loaded end, and the load is thus reduced to a real scalar value measuring the ratio of velocity over acoustic pressure. For a given engine geometry and a given temperature ratio between heater and cooler, numerical simulations of the active cell show that depending on the load value, the engine will or will not start. From the numerical results, for any given configuration, a critical temperature ratio is thus determined, corresponding to the onset of thermoacoustic oscillations, together with the frequency of the corresponding, most unstable mode. The analysis is performed using a time dependent non-linear model that takes into account two-dimensional effects as well as multi-frequency content. Finally, the influence of the load on the starting phase of the engine is discussed and the results are compared, both with results derived from the linear theory and with Atchley's experiments[8], bringing new insight on the engine-load coupling.

II. Physical model

A. Low Mach number approximation

The geometry consists of a long tube with length $\tilde{L}_{res}$, within which an active cell is placed, at a distance $\tilde{L}_L$ from the left end. The active cell consists of a stack of horizontal

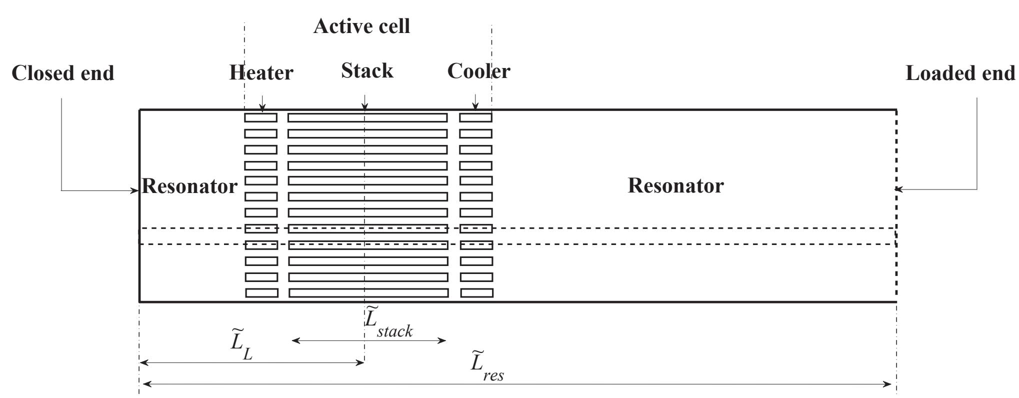

Figure 1: Simplified geometry of a thermoacoustic engine.

solid plates with length $\tilde{L}_{stack}$, placed between two heat exchangers also consisting of solid horizontal plates that have the same periodicity as the stack (see Figure 1). The geometry can then be reduced to a domain consisting of two half-plates plus the gap between them, plus a region that extends away from the solid plates.

First, a dimensionless coordinate system $\hat{x}$ is introduced, that resolves the acoustic aspect of the device, which is thus scaled by the resonator length $\tilde{L}_{res}$. The inert resonator end located at $\hat{x} = -\hat{l}_L = -\tilde{L}_L/\tilde{L}_{res}$ is a closed end. The second resonator end consists of a load placed at a fixed location $\hat{x} = \hat{l}_R = 1 - \hat{l}_L$, described in more detail below. The active cell is positioned at $\hat{x} = 0$. It has negligible size when scaled by $\tilde{L}_{res}$, as discussed below (see Figure 2a).

Next, a different dimensionless coordinate system (x, y) is introduced, that characterizes the active cell geometry, where lengths are scaled by the stack length $\tilde{L}_{stack}$, in both x and y. The corresponding dimensionless geometrical parameters include the vertical gap or flow passage between two stack plates h, the stack porosity h/H, where H is the domain height, equal to the vertical gap plus the thickness of one stack plate, the vertical gap between two heat exchanger plates h_x, the horizontal gap between heat-exchangers and stack L_{xs}, and the heat-exchanger lengths L_{hx} and L_{cx} (see Figure 2b).

The low Mach number model is described in detail in previous work[22]. The model assumes that the particle displacement spans a length of the order of $\tilde{L}_{stack}$, hence typical velocities of the order of $\tilde{U}_{ref} = \tilde{L}_{stack}/\tilde{\tau}$, where $\tilde{\tau}$ is of the order of the fundamental acoustic period of the empty resonator, $\tilde{\tau} = \tilde{L}_{res}/\tilde{c}$ and $\tilde{c}$ is the speed of sound. A reference Mach number $M = \tilde{U}_{ref}/\tilde{c}$ can then be introduced which also equals $M = \tilde{L}_{stack}/\tilde{L}_{res}$. In the following, the Mach number is assumed to be small or equivalently the stack is then taken to be much shorter than the resonator. The active cell size is then negligible in the $\hat{x}$ coordinate system.

Flow in the resonator is then described by linear acoustics. The solutions are expressed as a pair of planar traveling waves that move respectively left and right at the speed of sound. The two Riemann invariants $\mathcal{L}(\hat{x}, t)$ and $\mathcal{R}(\hat{x}, t)$ are used, defined by

$$\mathcal{L} = \gamma u - \sqrt{T}p', \quad \mathcal{R} = \gamma u + \sqrt{T}p' \tag{1}$$

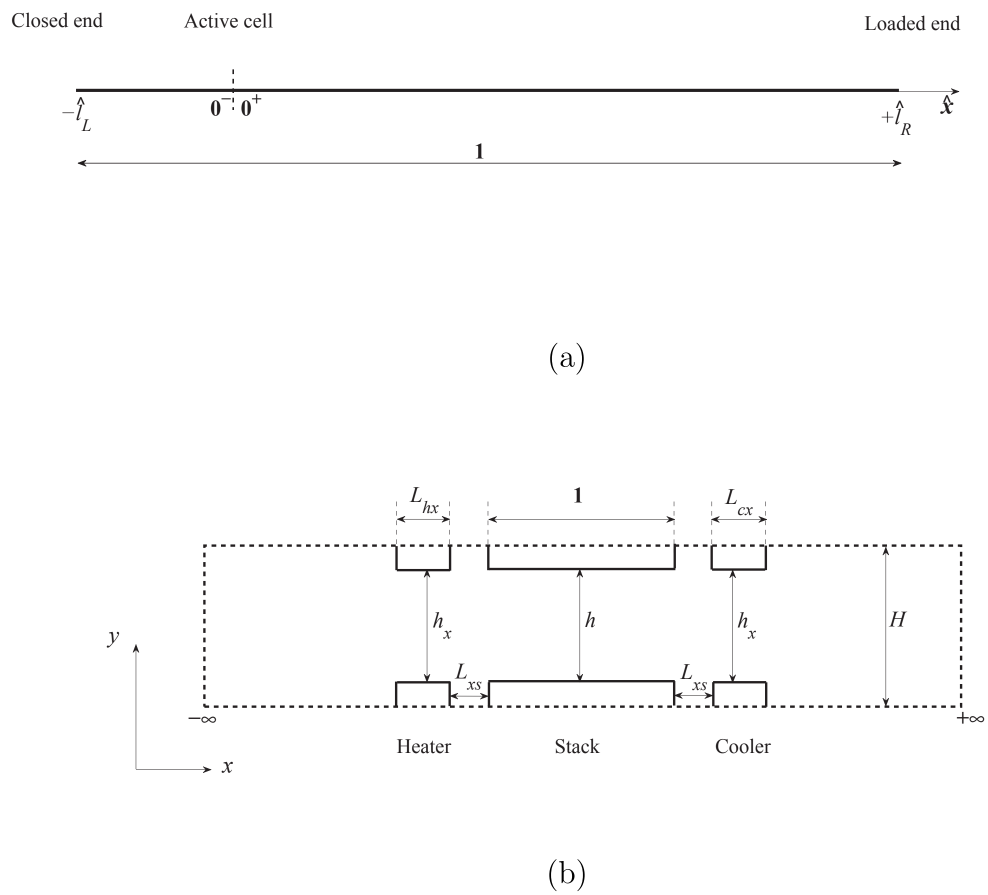

Figure 2: Geometry of resonator (a) and of active cell geometry (b) in dimensionless coordinates.

with γ the ratio of specific heats, $u(\hat{x}, t)$ the dimensionless gas velocity, T the dimensionless temperature (using the cold temperature as a reference) which is assumed constant in each resonator part ($T = T_h$ on the left side of the active cell, and $T = T_c = 1$ on the right side), and $p'(\hat{x}, t)$ the dimensionless order M (acoustic) pressure (using the mean gas pressure as a reference). At each tube end, the boundary condition results in a relationship that determines the outgoing wave as a function of the incoming wave, as explained in[22]. The order M pressure and acoustic velocity on both sides of the active cell ($\hat{x} = 0^{\pm}$) are expressed using these same quantities at previous times accounting for propagation on each side and reflections at the respective ends. The specific treatment of the loaded end will be described in detail in the next section.

Flow in the active cell is described by two-dimensional Navier-Stokes equations, with order M^2 pressure gradients superimposed to a pressure spatially uniform up to order M, and varying density and temperature. The solid stack plate problem is described by the heat conduction equation. In the stack and heat exchanger plates, physical properties such as density, thermal conductivity, heat capacity are taken to be constant. Thermal conductivity and heat capacity of the gas are also constant, with values corresponding to cold temperature, chosen as the reference temperature. Reference density of the gas is that corresponding to the reference (cold) temperature and the mean gas pressure.

At the solid-gas boundaries, continuity of temperature and heat flux are imposed, as well as a no slip condition. In the heat exchangers, uniform, constant temperatures are imposed with dimensionless values $T_c = 1$ in the cooler plates, $T_h > 1$ in the heater plates. Given the periodicity, open active cell boundaries are effectively adiabatic.

Boundary conditions at the open ends of the active cell are provided by appropriate matching of the inner (active cell) and outer (resonator) solutions. The latter are expressed using the Riemann invariants $\mathcal{L}$ and $\mathcal{R}$ defined by Eq. 1, traveling respectively left and right in the resonator, at the speed of sound. At each extremity of the active cell, the outgoing invariant is determined as a function of the incoming one, taking the corresponding resonator boundary conditions into account. These consist respectively of a zero velocity at the closed end, and the load described below in section B at the loaded end[22]. Finally, a global energy balance over the active cell relates velocities at the two cell extremities to heat transfer.

From the standpoint of resonator acoustics, the active cell is transparent to pressure but provides a source of volume. From the standpoint of the active cell, matching with the resonator occurs at infinity so that, in principle, the active cell has infinite length on both sides. However the numerical domain has to be finite. Its length is chosen equal to 5 times the stack length, which ensures proper matching, as confirmed by validation. The dimensionless parameters characterizing the problem are then the reference Mach number M, the relative position of the active cell in the resonator $\hat{l}_L$, parameters describing the geometry of the active cell (H, h_s, h_x, L_{xs}, L_{hx}, L_{cx}), a Péclet number $P_e = \tilde{U}_{ref}\tilde{H}/\tilde{\alpha}_{ref}$ where $\tilde{\alpha}_{ref}$ is the reference thermal diffusivity, a Reynolds number $R_e = \tilde{\rho}_{ref}\tilde{U}_{ref}\tilde{H}/\tilde{\mu}_{ref}$, $\tilde{\rho}_{ref}$ and $\tilde{\mu}_{ref}$ being the reference density and viscosity, and the Péclet number $P_{es} = P_e\,\tilde{\alpha}_{ref}/\tilde{\alpha}_s$ in solid walls, where $\tilde{\alpha}_s$ is the thermal diffusivity of the solid material.

B. Load model

The present study considers a purely resistive load, so that instantaneous acoustic pressure $p'(\hat{l}_R, t)$ and velocity $u(\hat{l}_R, t)$ at the loaded end are assumed to be in phase. The load is thus characterized by a scalar value equal to the ratio of dimensionless acoustic pressure to velocity, i.e. $f = p'(\hat{l}_R, t)/\,u(\hat{l}_R, t)$, with f a positive real. Such a load behaves as a pure resistance in the electrical analogy. Actual loads may include inertial and capacitance effects; these will depend not only on mechanical design, but also on the driven devices. A detailed study of these issues is beyond the scope of the present work.

The limit value $f \to 0$ corresponds to an open end, with $p'(\hat{l}_R, t) = 0$, while the limit value $f \to \infty$ corresponds to a closed end, with $u(\hat{l}_R, t) = 0$.

The boundary condition at the load location $\hat{x} = \hat{l}_R$ is carried along the returning (left-moving) characteristic, resulting in the corresponding boundary condition at the right end of the active cell, at $\hat{x} = 0^+$. Specifically, the boundary condition at $\hat{x} = 0^+$ relates the current local value of the left-moving Riemann invariant and the value of the right-moving Riemann invariant at the same location but at a previous time that differs by the round trip time between the active cell and the load at the speed of sound $\sqrt{T_c}$:

$$\mathcal{L}(0^+, t) = Z\mathcal{R}(0^+, t - 2\hat{l}_R/\sqrt{T_c}) \tag{2}$$

in which a real coefficient Z was introduced, defined as:

$$Z = \frac{\gamma - f}{\gamma + f}. \tag{3}$$

While f goes from zero for an open end to infinity for a closed end, Z has the finite span from -1 for a closed end to $+1$ for an open end. Furthermore, the expression emphasizes the particular value $f = \gamma$, for which Z vanishes, corresponding to a left-moving Riemann variable with zero value, regardless of the right-moving variable, hence to a non-reflecting load. If $Z = 0$, the solution no longer depends upon the length of the right side of the resonator; such a load may be difficult to implement, and of little practical value, as results below will confirm; however, that case still has some interest as it separates different regimes. In the framework of the harmonic approximation, it is possible to relate f or Z to the reflection coefficient at the loaded end hence to the standing wave ratio[23]. In that context the absolute value of Z is equal to the modulus of the reflection coefficient. The limit values $Z = \pm 1$ correspond to a pure standing wave in the resonator, while the limit case $Z = 0$ corresponds to a pure traveling wave moving from the active cell towards the load. Between those limit cases, the wave is a combination of two waves traveling in opposite directions with unequal amplitudes, i.e. neither standing or purely traveling. In the current study, however, the effect of the load parameter on starting performance will be investigated in the time domain with no a priori on the nature of the wave developing in the engine. Critical temperature ratio between heater and cooler and starting frequencies will be analyzed by varying the value of f in the range 0 to $+\infty$. Results will be more conveniently shown as functions of the coefficient Z in the range $[-1, 1]$.

III. Numerical simulation

A. Algorithm

The problem in the active cell is solved numerically using a finite volume code[22]. Diffusion is dealt with implicitly while advection is explicit. The scheme is second-order accurate in space and in time. A fractional time step projection method adapted for variable density is used to enforce continuity. The ADI algorithm is used to solve the Helmholtz equation for time advance of temperature and velocities. A multigrid algorithm determines the pressure correction. Solutions of the coupled equations providing velocity boundary conditions and acoustic pressure at the active cell location from resonator acoustics and energy balance are appropriately integrated in the solution sequence[22].

B. Procedure

Simulations account for a specific engine geometry, characterized by the reference Mach number M, the relative distance of the active cell to the left end $\hat{l}_L$ and the dimensions of the active cell H, h, h_x, L_x and L_{xs}. Most of the current results were obtained for L_{xs} equal to h. Reference Péclet number P_e, solid Péclet number P_{es}, Reynolds number R_e are maintained constant. The evolution in time of the velocity and temperature fields is computed for given heater and cooler temperatures and load. The required initial conditions consider fluid at rest and temperature profiles, obtained numerically, corresponding to steady conduction in the walls and in fluid at rest. Initial conditions also need being specified for resonator acoustics, and these need being nonzero since the steady solution to the global problem consists of fluid at rest, together with a stationary conduction solution. To that effect, and in order not to favor specific modes, an initial random noise is imposed in the resonators. Small $\mathcal{O}\left(10^{-4}\right)$ random values are thus assigned to the Riemann invariants at the active cell entrance and exit for a time window prior to zero, of length equal to the round trip time between active cell and the respective resonator end.

Starting from initial conditions specified above, the velocity $u(x, y, t)$, dynamic pressure $p(x, y, t)$, temperature $T(x, y, t)$ and density $\rho(x, y, t)$ fields are calculated inside the active cell at each time step. Coupling at the active cell entrance and exit provides the velocity at the entrance $u(0^-, t)$ and exit $u(0^+, t)$ of the active cell, as well as the value of the acoustic pressure at the active cell location $p'(0, t)$ at each time step. The velocity values at the entrance and exit of the active cell serve as boundary conditions for velocity inside the active cell. The order M acoustic pressure $p'(0, t)$ which is included in the active cell model only through boundary conditions is an outcome of the simulation. This quantity is analyzed here to characterize the device's regime : motion damping or amplification.

C. Post-processing

Acoustic modes are characterized by amplitude and complex frequency, i.e. frequency and growth rate. If the temperature ratio between heater and cooler is small, growth rates are all negative i.e. the amplitudes of all modes decrease in time and motion stops. A critical temperature ratio is obtained when one of the modes exhibits positive growth: instability occurs and the device starts. In order to find the critical temperature ratio $T_{crit} = \tilde{T}_{hcrit}/\tilde{T}_c$ for a given load, repeated simulations are performed for increasing values of the hot temperature, until a first growth rate becomes positive.

The pressure signal $p'(0,t)$ is analyzed to extract the growth rate and frequency of the dominant modes, by fitting the signal to an approximation of the form:

$$p'(0,t) = \sum_{i=1}^{n} A_i e^{\sigma_i t} \cos(\omega_i t) + B_i e^{\sigma_i t} \sin(\omega_i t) \tag{4}$$

where n is the desired number of modes, with typical value 4. The fitting uses a window that includes m consecutive data points, collected after several reference periods have elapsed so that a dominant exponential mode has emerged from the initial phase affected by initial conditions. In Expression (4), σ_i is the growth rate of mode i, ω_i is its angular frequency, and A_i, B_i are amplitudes.

Fitting the $(A_i, B_i, \sigma_i, \omega_i)$ coefficients is performed using an iterative two stage procedure. Starting with an initial guess (σ_i, ω_i), the (A_i, B_i) coefficients are determined by least mean square error minimization, using the m data points. Then the (σ_i, ω_i) coefficients are obtained using a simplex algorithm. Iterations continue until the fit satisfies a given criterion, with the quadratic error below some adequate lower bound. The whole procedure is iterated until an error below 10^{-4} on (σ_i, ω_i) is reached.

IV. Results

A. Conditions

Numerical simulations were carried out on an existing prototype of thermoacoustic engine[22], with a "short" thermoacoustic active cell inserted in a long resonator closed at both ends. The engine is modeled as the simplified device introduced in Figure 2, assuming acoustics is lossless in the resonators and concentrating all dissipation at the loaded end.

The working fluid is helium. The dimensions (resonator length, stack length, distance between the left end and the active cell, plate spacing) and the conditions of the experiments, such as mean pressure and cold temperature, are kept constant. The relevant dimensionless parameters are summarized in Table 1, and the relevant fluid properties are summarized in Table 2.

Numerical simulations were carried out using a regular two-dimensional mesh for the active cell, with either 2048×32 or 4096×64 grid points. The simulation domain is long enough to ensure that the flow velocity near the entrance and exit is parallel to the resonators. The time step is adjusted in order to satisfy the numerical stability condition, with about 200 (coarse grid) to 2000 (fine grid) time steps per reference acoustic period. Typically only 60 min of CPU time are necessary for each numerical run (about 100 periods), such as the one shown in Figure 3.

For given load value and given heater temperature, the time history of acoustic pressure in the active cell was recorded from the computation. An example of the time signal is shown in Figure 3(a). The first oscillations are rather erratic (details are not shown in Figure 3(a) and they depend upon initial conditions. The signal eventually becomes smoother and amplitudes appear to correspond to a superimposition of exponentially varying modes. The signal appears to remain multi-frequency. This is confirmed in Figure 3(b) which shows the corresponding spectrogram. In the figure, the angular frequency is scaled by a reference angular frequency ω_{ref} equal to the fundamental angular frequency of the empty resonator closed at both ends, filled with gas at a mean pressure $\tilde{P}_m$ and a temperature equal to the cold temperature $\tilde{T}_c$. At any given time, the power spectrum exhibits successive peaks corresponding to the resonant frequencies of the engine for the specific load value. As time evolves, most modes are damped while some are amplified. A more accurate determination of the frequencies and growth rates of the dominant modes is presented in the next section.

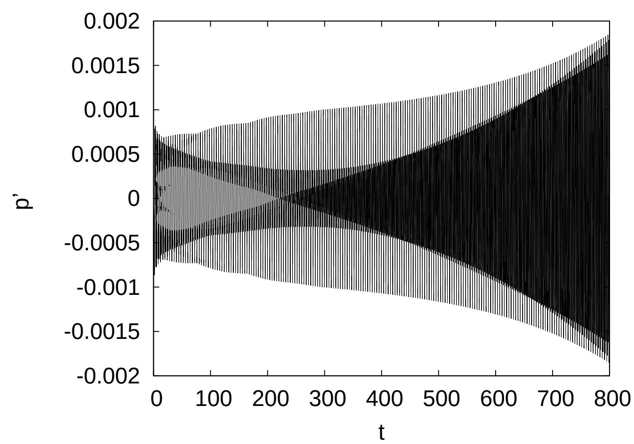

(a)

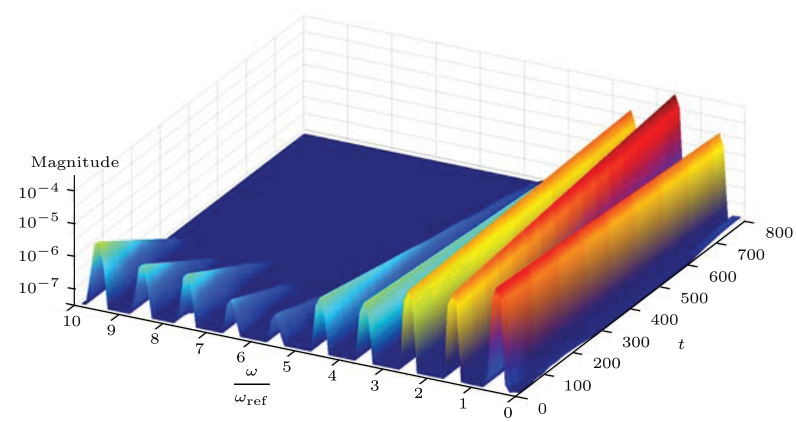

(b)

Figure 3: (a) Typical time signal of acoustic pressure $p'(0,t)$, and (b) (color online) associated spectrogram (the magnitude is the square root of the power density spectrum). $Z = 0.988$. $T_h = 1.08$.

B. Results at a given active cell location

First, the effect of the load on the critical temperature ratio is studied, for a single active cell location.

Analyzing the pressure signal using the approach described in Section , the growth rate and frequency of the four dominant modes are calculated, for a range of increasing values of the temperature of the heater T_h, for a given load f, until unstable modes appear. The most unstable mode is identified as the first mode for which the growth rate σ goes from negative to positive, as T_h is increased. Plotting σ as a function of the dimensionless temperature T_h helps identifying the precise value of the critical temperature ratio, as Figure 4 shows. In the vicinity of the critical value, σ varies nearly linearly with T_h, and a precise determination of the critical temperature ratio is obtained by interpolation. For example in Figure 4, the critical temperature ratio is found to be $T_{crit} = 1.845$.

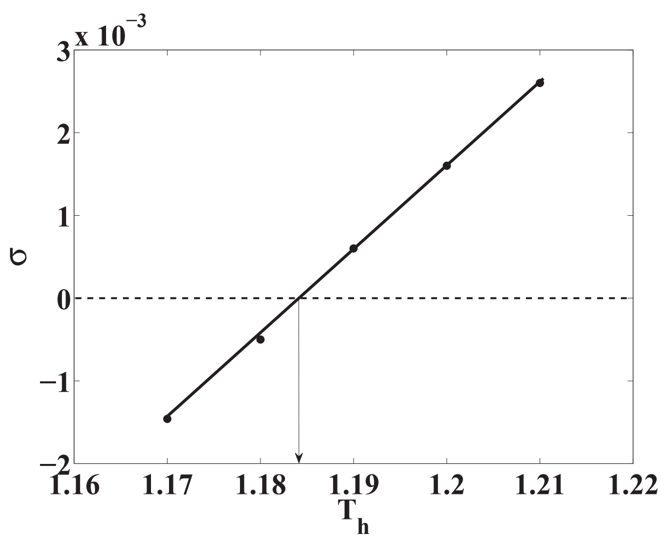

Figure 4: Growth rate of most unstable mode as a function of the hot exchanger temperature, $Z = -0.963$.

Next, varying the load and reproducing the same procedure for each load value results in a stability diagram (Figure 5) in the (Z, T_h) plane showing stable and unstable zones. The zones are separated by a stability curve connecting all the critical temperature ratios causing the engine to start. The region above the stability curve corresponds to instability. Figure 5 shows a stability domain roughly delimited by a symmetrical triangle peaking at $Z = 0$, when a semi-log scale is used.

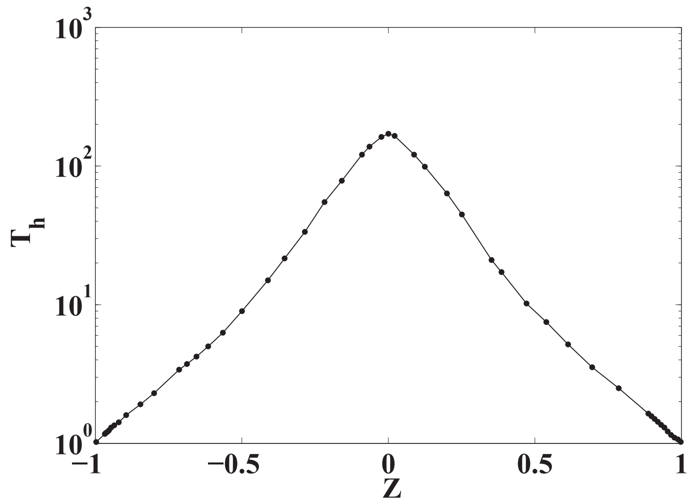

Figure 5: Stability diagram in the (Z, T_h) plane, showing the stability curve -●-. The region above the curve corresponds to instability.

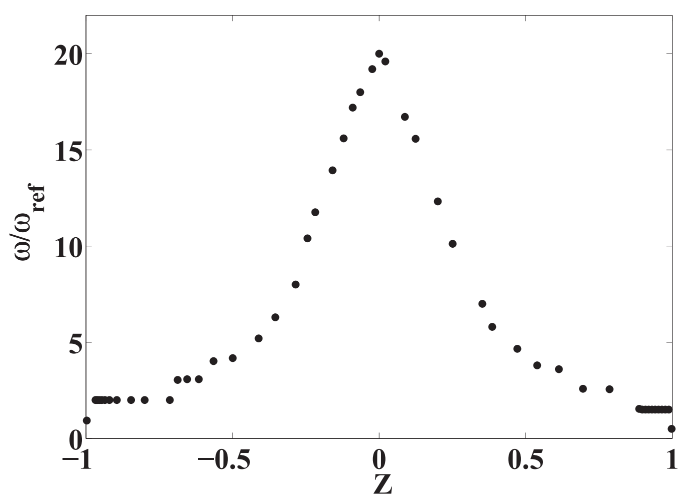

Figure 6: Angular frequency of the most unstable mode scaled by ω_{ref}, as a function of Z.

Figure 6 shows the angular frequency ω of the first mode to become unstable as a function of Z. As $|Z|$ decreases, the frequency of the most unstable mode is observed to increase. Although the general shape of the curve is approximately symmetrical as it is in Fig. 5 for the critical temperature, the values of ω do not display any symmetry. Indeed, critical modes near $Z = -1$ are of the closed-end type (multiples of $\lambda/2$) whereas critical modes near $Z = 1$ are of the open-end type (odd multiples of $\lambda/4$). This results in distinct sets of onset frequencies, as is further discussed and analyzed in Sections IV.C. and V when commenting on Figures 7, 8 and 11.

For Z close to zero, Figure 5 shows a very large critical temperature ratio, too large for being realistic. Likewise, frequencies become very high so that resolution, both of the wavelength in space, and of the period in time, becomes quite poor. Furthermore, these curves were obtained assuming constant viscosity and thermal conductivity conditions, which is unrealistic at high temperature. These results are thus somewhat dubious, and therefore, Figure 5 merely gives a qualitative picture for Z close to zero. While such numerical critical temperature ratios may be of limited value, the conclusion is valid that in the vicinity of $Z = 0$ the device will not start for any realistic temperature ratio (T_h less than about 10), all modes remaining stable.

C. Results varying the active cell location or configuration

The stability diagrams shown in Figures 5 and 6 can be used, for a given configuration, to predict the critical temperature ratio and the dominant frequency as a function of the load.

These diagrams are modified if the location of the active cell measured by $\hat{l}_L$ is varied. The stability curve becomes a stability surface, which can be used to predict the critical temperature ratio for a given setup. For given load and heater temperature values, the position of the active cell has to be within a certain region for the engine to start. For an active cell outside this region, all modes are dampened and the engine will not start.

Figure 7 shows the growth rate of the fundamental mode and of the first harmonic as a function of the active cell location for $Z = -0.963$ and $T_h = 1.2$. It is found that if the active cell is positioned at $0.083 < \hat{l}_L < 0.12$ the first harmonic is the most unstable mode. In contrast, if it is placed at $0.12 < \hat{l}_L < 0.43$ the fundamental mode is dominant. For that parameter settings, the overall optimal position for starting performance is $\hat{l}_L = 0.27$, for which the growth rate is maximum. Another way to address the issue is to determine the active cell location for which the critical temperature ratio is minimum. Figure 8 shows the value of the critical temperature ratio for varying active cell locations and for selected load values. Figure 8(a) shows results for negative values of Z near $Z = -1$, in which case both ends are closed. For each value of Z, there is one stack position that minimizes the critical temperature ratio. The optimal position is approximately 0.25 for $Z = -0.99$. Since the fundamental mode (the $\lambda/2$ mode) is the critical one in that region, this corresponds to a stack located at $\lambda/8 \simeq \hat{L}_{res}/4$ as expected ($\hat{L}_{res} = 1$). As Z departs from $Z = -1$ the wavelength increases so that the optimal position shifts towards the center of the resonator.

Figure 8(b) corresponds to positive values of Z, near $Z = 1$, for which the cold end is open. The optimal position is approximately 0.16 for $Z = 0.99$. Now the first harmonic (the $3\lambda/4$ mode) is the critical mode in that range of stack locations. This corresponds to a stack located at $\lambda/8 \simeq \hat{L}_{res}/6 \approx 0.17$. For decreasing values of Z, below $Z = 1$, the wavelength increases so that the optimal position again shifts towards the resonator center. Note that here the active cell is located at $\hat{l}_L \leq 0.25$. If the stack were placed further away, the fundamental mode would become the critical one and the optimal position would shift towards 0.5.

The effect of varying the distance between the heat exchangers and the stack L_{xs} was also studied. In all previous cases the horizontal spacing L_{xs} was equal to the vertical stack plate spacing h. Figure 9 shows the stability diagram for two other situations: for heat-exchangers and stack in direct contact ($L_{xs} = 0$) and doubling the horizontal spacing ($L_{xs} = 2h$). While placing the heat-exchangers and stack in contact together results in significant reduction of the critical temperature ratio for all values of the load (potentially leading to a significant increase in longitudinal conduction losses), the effect of doubling the

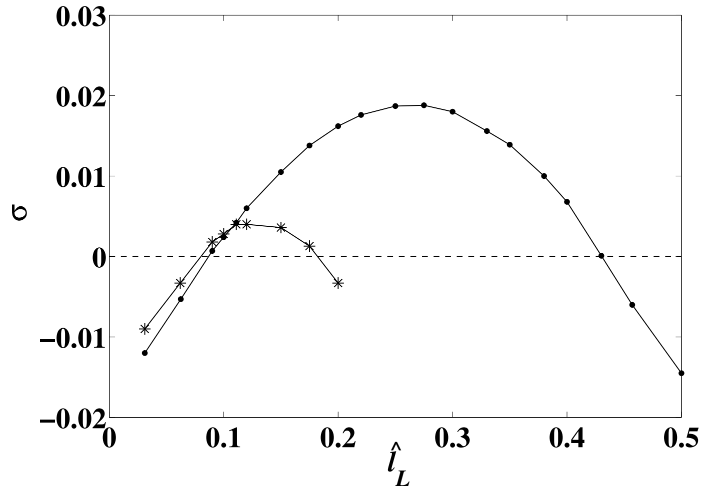

Figure 7: Growth rates as a function of the active cell location for $0 < \hat{l}_L < 0.5$, $Z = -0.963$, $T_h = 1.2$. -•- fundamental mode (the $\lambda/2$ mode), -*- first harmonic mode (the λ mode).

spacing is insignificant. The nature of the critical modes will be discussed in the next section (see comments of Figure 11 in Section V. below).

V. Comparison with the linear theory

In this section the critical temperature ratio associated to a given acoustic mode is estimated following Rott's linear theory [5;24], which is outlined here using dimensional values for the various parameters. Linear results were obtained for a slightly different configuration, with same total resonator length, stack length and position of the stack center within the resonator as above. However the detailed heat exchanger geometry used above was replaced by imposing a linear wall temperature profile in the stack and constant mean temperatures $\tilde{T}_h$ on the left side of the stack, and constant mean cold temperature $\tilde{T}_c$ on the right side.

The flow in the resonator tubes left and right of the stack was taken as one-dimensional isentropic linear acoustics with different speeds of sound corresponding to the respective temperatures $\tilde{T}_h$ and $\tilde{T}_c$. The boundary conditions on the left and right ends were the same as previously, with a load modeled as a real impedance $\tilde{R}$ relating acoustic velocity and acoustic pressure. The acoustic pressure and velocity amplitudes ($\tilde{p}'_h(\tilde{x})$, $\tilde{u}_h(\tilde{x})$) on the

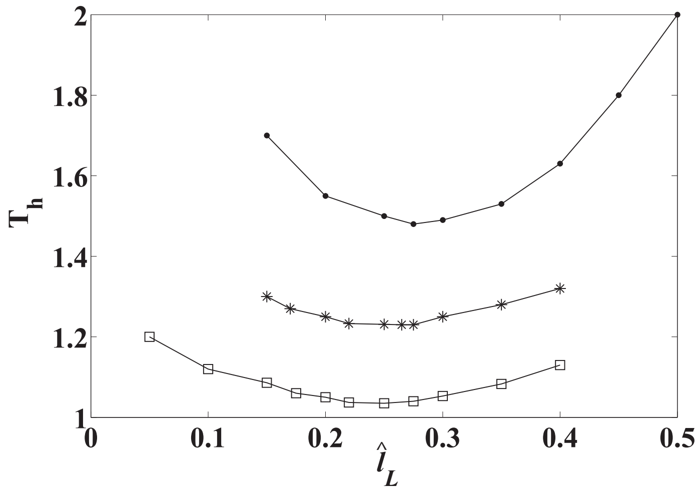

(a)

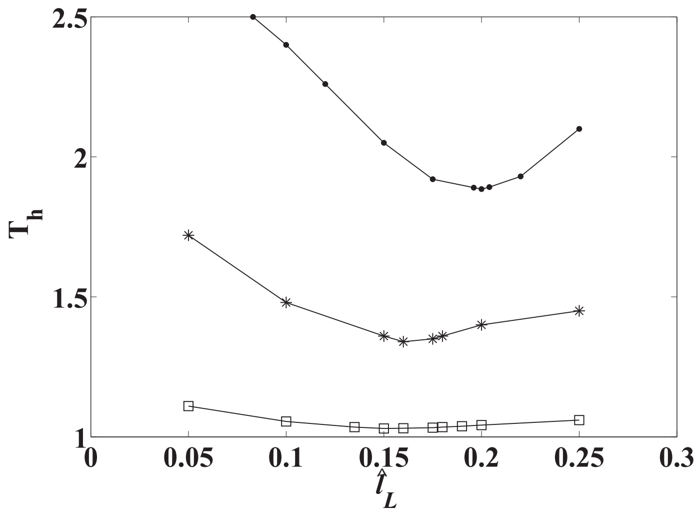

(b)

Figure 8: Stability diagram showing the critical temperature ratio as a function of the active cell location for (a) $-\square-$ $Z = -0.99$, $-\ast-$ $Z = -0.92$, $-\bullet-$ $Z = -0.85$, the critical mode is the fundamental mode ($\lambda/2$), and (b) $-\bullet-$ $Z = 0.79$, $-\ast-$ $Z = 0.90$, $-\square-$ $Z = 0.99$, the critical mode is the first harmonic ($3\lambda/4$).

left resonator part and $(\tilde{p}'_c(\tilde{x}), \tilde{u}_c(\tilde{x}))$ on the right resonator part are functions of position which can be expressed simply in terms of two unknowns, namely the complex maximum amplitudes $\tilde{U}_h$ and $\tilde{U}_c$.

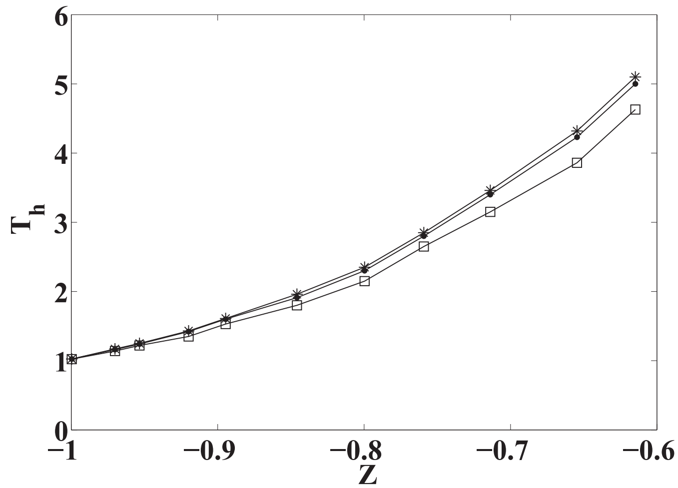

(a)

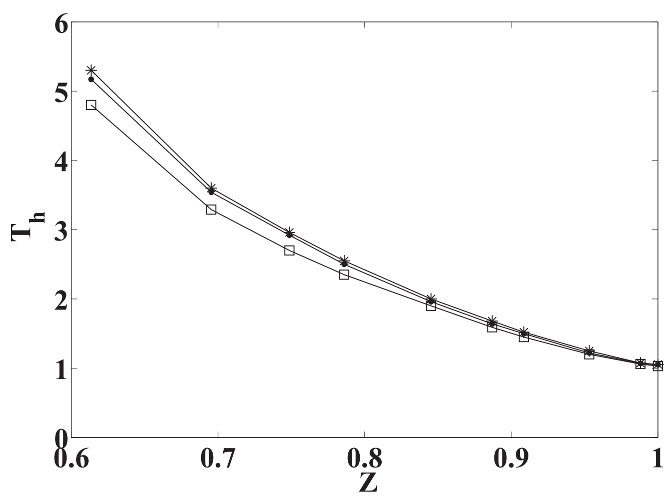

(b)

Figure 9: Stability diagram in the (Z, T_h) plane, showing the stability curve (critical temperature ratios) for three distances between heat-exchangers and stack, —□— $L_{xs} = 0$, —•— $L_{xs} = h$, —∗— $L_{xs} = 2h$. (a) $-1 < Z < -0.6$, (b) $0.6 < Z < 1$.

The stack region is described as a two-dimensional channel of height $2\tilde{y}_0$ equal to the vertical distance between stack plates, extending from $\tilde{x} = 0$ to $\tilde{x} = \tilde{L}_{stack}$. Following Rott's approach, solutions of the viscous flow equations are sought for as harmonic functions in time with angular frequency $\tilde{\omega}$, using a boundary layer approximation and integrating vertically over the channel height. Also, the stack is assumed to be acoustically compact, so that the acoustic pressure amplitude $\tilde{p}'$ is homogeneous through the stack. Since temperature varies linearly through the stack, $\dfrac{d\tilde{T}}{d\tilde{x}}$ is a constant.

The resulting dimensional equation for the acoustic velocity in Fourier space is[25]:

$$\frac{d\tilde{u}_1}{d\tilde{x}} - \frac{\tilde{f}_\kappa - \tilde{f}_\nu}{(1-\tilde{f}_\nu)(1-P_r)} \frac{1}{\tilde{T}} \frac{d\tilde{T}}{d\tilde{x}} \tilde{u}_1 = -\frac{i\tilde{\omega}}{\gamma \tilde{P}_m} \left[1 + (\gamma - 1)\tilde{f}_\kappa\right] \tilde{p}' \tag{5}$$

where $\tilde{P}_m$ is the gas mean pressure, Rott's factors are defined as

$$\tilde{f}_\nu = \frac{\tanh\left[(1+i)\tilde{y}_0/\sqrt{2\tilde{\mu}/(\tilde{\rho}\tilde{\omega})}\right]}{(1+i)\tilde{y}_0/\sqrt{2\tilde{\mu}/(\tilde{\rho}\tilde{\omega})}}, \quad \tilde{f}_\kappa = \frac{\tanh\left[(1+i)\tilde{y}_0/\sqrt{2\tilde{k}/(\tilde{\rho}\tilde{c}_p\tilde{\omega})}\right]}{(1+i)\tilde{y}_0/\sqrt{2\tilde{k}/(\tilde{\rho}\tilde{c}_p\tilde{\omega})}} \tag{6}$$

with constant gas properties $\tilde{\mu}$, $\tilde{c}_p$, $\tilde{k}$ (therefore the Prandtl number P_r is constant also) and density $\tilde{\rho}$ depending on position through variation of temperature. The $\tilde{f}_\nu$ and $\tilde{f}_\kappa$ factors are functions of $\tilde{x}$. Equation 5 is a first order linear inhomogeneous equation, so that the solution is expressed as :

$$\begin{aligned}\tilde{u}_1(\tilde{x}) = \exp\left[\int_0^{\tilde{x}} \frac{\tilde{f}_\kappa(\tilde{x}_1) - \tilde{f}_\nu(\tilde{x}_1)}{(1-\tilde{f}_\nu(\tilde{x}_1))(1-P_r)} \frac{1}{\tilde{T}(\tilde{x}_1)} \frac{d\tilde{T}}{d\tilde{x}_1} d\tilde{x}_1\right] \times \\ \left\{C_1 - \int_0^{\tilde{x}} \frac{i\tilde{\omega}}{\gamma\tilde{P}_m}\left[1 + (\gamma-1)\tilde{f}_\kappa(\tilde{x}_1)\right] \tilde{p}' \exp\left[-\int_0^{\tilde{x}_1} \frac{\tilde{f}_\kappa(\tilde{x}_2) - \tilde{f}_\nu(\tilde{x}_2)}{[1-\tilde{f}_\nu(\tilde{x}_2)](1-P_r)} \frac{1}{\tilde{T}(\tilde{x}_2)} \frac{d\tilde{T}}{d\tilde{x}_2} d\tilde{x}_2\right] d\tilde{x}_1\right\}\end{aligned} \tag{7}$$

in which C_1 is an integration constant.

That expression can be rewritten using the relationship between position and temperature, as:

$$\begin{aligned}\tilde{u}_1(\tilde{x}) = \exp\left[-\int_{\tilde{T}(\tilde{x})}^{\tilde{T}_h} \frac{\tilde{f}_\kappa(\theta) - \tilde{f}_\nu(\theta)}{[1-\tilde{f}_\nu(\theta)](1-P_r)} \frac{1}{\theta} d\theta\right] \times \\ \left\{C_1 + \int_{\tilde{T}(\tilde{x})}^{\tilde{T}_h} \frac{i\tilde{\omega}}{\gamma\tilde{P}_m}\left[1 + (\gamma-1)\tilde{f}_\kappa(\theta)\right] \tilde{p}' \exp\left[\int_\theta^{\tilde{T}_h} \frac{\tilde{f}_\kappa(\theta^*) - \tilde{f}_\nu(\theta^*)}{[1-\tilde{f}_\nu(\theta^*)](1-P_r)} \frac{1}{\theta^*} d\theta^*\right] \frac{\tilde{L}_{stack}}{\tilde{T}_c - \tilde{T}_h} d\theta\right\}\end{aligned} \tag{8}$$

Boundary conditions are provided by matching with resonator acoustics. While the resonator acoustics yield velocities uniform transversally, the boundary layer model incorporated in the linear theory used in the stack results in a specific nonuniform velocity profile.

Matching the mean velocities values is justified based upon a multiple length approach similar to that used above. Indeed the transition region is small compared with acoustic lengths, so that mass and pressure corrections due to the transition zone occur at higher order. For known boundary conditions at the outer resonator ends, acoustics yield a relationship between acoustic pressure in the stack, $\tilde{p}'$, and the uniform acoustic velocities $\tilde{U}_h$ and $\tilde{U}_c$, respectively on the left and right side. Continuity conditions require mean velocities and acoustic pressure to match at both stack ends.

Requiring the resulting globally homogeneous problem to have non-trivial solutions results in a dispersion relation that cannot be solved in closed form for the complex frequency ω. A numerical solution was thus implemented using a shooting method, integrating over the stack length, and iterating until the relationship between pressure and velocity at the end match the acoustic boundary condition. The method requires an initial guess for the complex frequency, conveniently provided by the numerical results of section .

Figures 10 and 11 show a comparison between numerical results and results obtained using the linear theory. Only the range $|Z| > 0.6$ is shown, which contains all cases of practical interest.

In Fig. 10, the critical temperature ratio is shown as a function of Z. There is very good agreement between the two approaches, with the ratio obtained through the linear theory slightly above the numerical values, which may be ascribed to a shorter length for lossless acoustics in the linear approach. As $Z \to -1$, the critical temperature ratio becomes very close to one. For instance, for $Z = -0.997$, the critical temperature ratio is found to be $T_{crit} = 1.024$ numerically while linear theory gives $T_{crit} = 1.14$. Similarly for an almost open-end resonator, $Z = 0.998$, numerical simulations yield a value $T_{crit} = 1.025$, vs. $T_{crit} = 1.13$ from linear theory.

In Fig.11, the onset frequency normalized by ω_{ref} is shown as a function of Z for both approaches, showing again excellent agreement. Also plotted (continuous lines) are the resonant frequencies of a lossless resonator with a temperature discontinuity positioned at

$\hat{x} = 0$, for hot temperature T_h set to the critical value $T_{crit}(Z)$ determined by the simulation, for a closed right end in Fig. 11(a) or an open right end in Fig. 11(b). The small frequency increase as T_h increases is barely noticeable on the continuous (nearly horizontal) lines. The load itself has a small effect since the points from both numerical results and linear theory, and the points on the horizontal lines, which only take into consideration the changes in temperature due to Z, but not the values of Z itself only differ slightly. However the most visible effect of the load is the switch in the first mode to become unstable (and thus of the onset frequency), represented by vertical lines on Fig. 11. In Figure 11(a), each vertical range corresponds to a multiple of $\lambda/2$, and in Figure 11(b), each vertical range corresponds to an odd multiple of $\lambda/4$. As $|Z|$ diminishes, progressively higher frequency modes are the first to become unstable. For the current configuration, $|Z|$ has to be extremely close to one for a fundamental mode to be the first to become unstable. The results, both numerical and from linear theory, show that as $|Z|$ decreases, the wavelengths of each mode increase. Thus the position within the resonator maximizing power shifts away from the closed end, for each mode. Hence the optimal position of the active cell for destabilizing any mode ($\lambda_n/8$, $n = 1, 2, 3, ...$) shifts to the right, as was already shown on Figure 8. Mode n will remain the most unstable until $\lambda_n/8$ of the nth mode shifts too far away from the active cell location and $\lambda_{n+1}/8$ of the next mode becomes more favorably located, resulting in step increases in the frequency of the most unstable mode as shown in Fig. 11.

VI. Comparison with experimental results

In this section, numerical results from the current model are compared with the experimental results of Atchley et al.[8]. The experimental setup consists of a thermoacoustic cell that is about 6.5 cm long, with a 3.5 cm long stack, inserted inside a one meter long resonator closed at both ends, at about one tenth of its length, 0.87 m from the right end[26]. The inner radius of the resonator is 1.91 cm. Here its cross-sectional area is denoted by A. The only "load" on the engine is dissipation in the gas contained in the resonator (he-

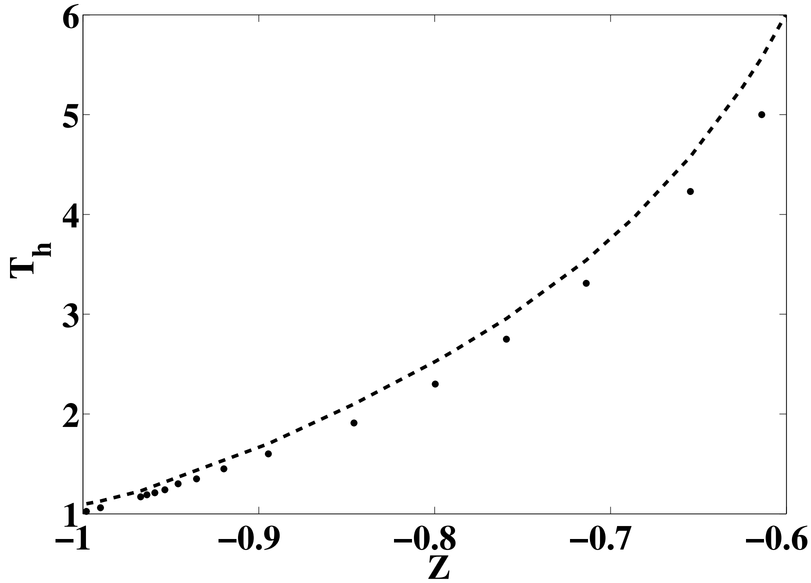

(a)

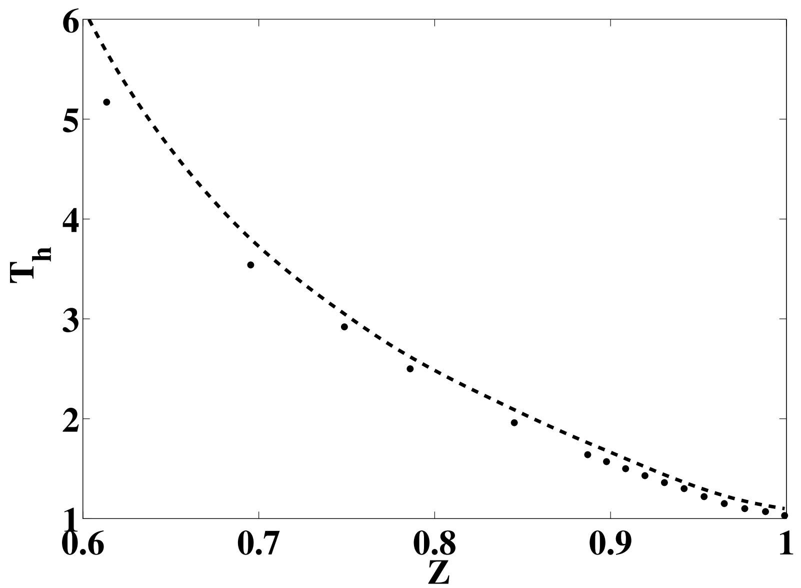

(b)

Figure 10: Stability diagrams in the (Z, T_h) plane, showing critical temperature ratios, • Numerical simulation, $---$ Linear theory. (a) $-1 < Z < -0.6$; (b) $0.6 < Z < 1$.

lium under pressure, initially at ambient temperature). The experiments[8] show that at low mean pressure the most unstable mode is the first harmonic, while at higher pressure the

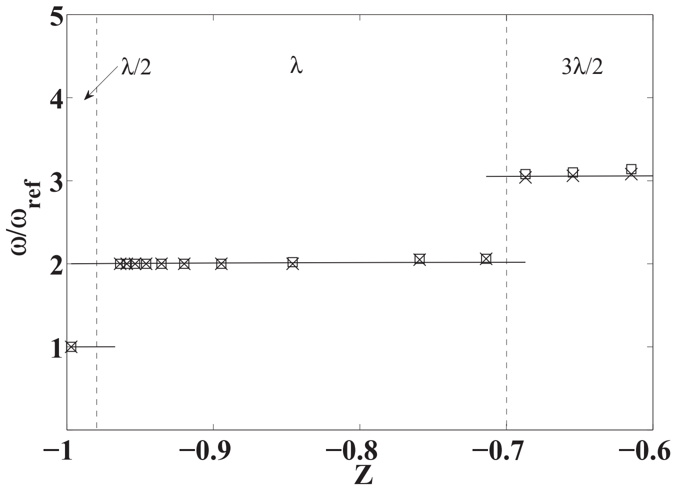

(a)

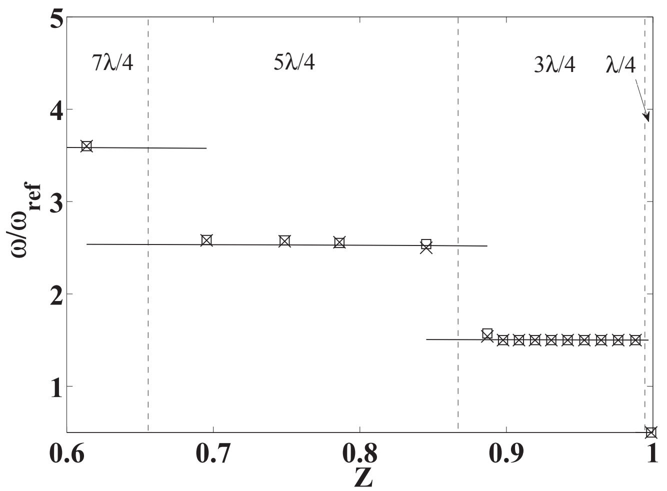

(b)

Figure 11: Frequency of the most unstable modes vs. Z. $\square$ linear theory, $\times$ simulations, (a) $-1 < Z < -0.6$; —— resonant frequencies of a closed-closed lossless resonator with temperature discontinuity at $\hat{x} = 0$ and $T_h = T_{crit}(Z)$ determined by numerical simulations, $---$ approximate vertical separation between modes (multiples of $\lambda/2$), (b) $0.6 < Z < 1$, —— resonant frequencies of an open-closed lossless resonator with temperature discontinuity at $\hat{x} = 0$ and $T_h = T_{crit}(Z)$, $---$ approximate vertical separation between modes (odd multiples of $\lambda/4$).

fundamental mode becomes the most unstable. There is also a region where both modes are unstable.

For comparison, simulations were thus performed for several mean pressure values. One of the model assumptions is that acoustics is lossless in the resonators, so that all dissipation is due to the load, while the experimental results[8] were obtained with no load but with losses. For comparison, the load value in the present model was identified such that the critical temperature ratio obtained by simulation matches the experiment. For $\tilde{P}_m = 0.44$ MPa, it is found that a dimensionless load value of $f = 45$ in the present model yields a critical heater temperature that coincides with the value obtained experimentally $\tilde{T}_h = 660$ K. That value corresponds to a dimensional resistive load value $\tilde{R} = fM\tilde{P}_m/(A\tilde{U}_{ref}) = 17.1$ MPa·s·m^{-3}. The mode that becomes unstable is the fundamental mode, which is also consistent with the experiments. As the heater temperature is increased in the simulation while keeping the load value constant, the first harmonic also becomes unstable when $\tilde{T}_h = 821$ K, which is again in agreement with the value $\tilde{T}_h \simeq 800$ K found in the experiment.

For $\tilde{P}_m = 0.15$ MPa, a load value $f = 16$ is necessary to reproduce the measured critical heater temperature $\tilde{T}_h = 718$ K, corresponding to dimensional value $\tilde{R} = 2.1$ MPa·s·m^{-3}. For that mean pressure value, the mode that first becomes unstable is the first harmonic, again in the experiments as well as in the present simulations. The load value that matches the experimental stability diagram of Atchley et al.[8], shown in Figure 12, is found to depend only on the mean pressure. In the electro-acoustic analogy, the cold resonator in the experimental configuration is a simple right-ended duct filled with helium prone to viscous and thermal dissipation. In the present model, the lossless resonator is connected to a purely resistive load, which is found to mainly play the role of a thermal resistance. Indeed the thermal resistance in the experiment may be estimated based on the classical expression[1], $R_\kappa = 2\gamma\tilde{P}_m/[\omega(\gamma - 1)S\delta_\kappa]$, where S is the surface area of the resonator side and δ_κ the thermal boundary-layer thickness. If $\tilde{P}_m = 0.44$ MPa (resp. 0.15 MPa), $\tilde{T}_{cold} = 293$ K, the thermal resistance is found to be of the order of 40 MPa·s·m^{-3} (resp. 5 MPa·s·m^{-3}). For $\tilde{P}_m$=0.15 MPa, the

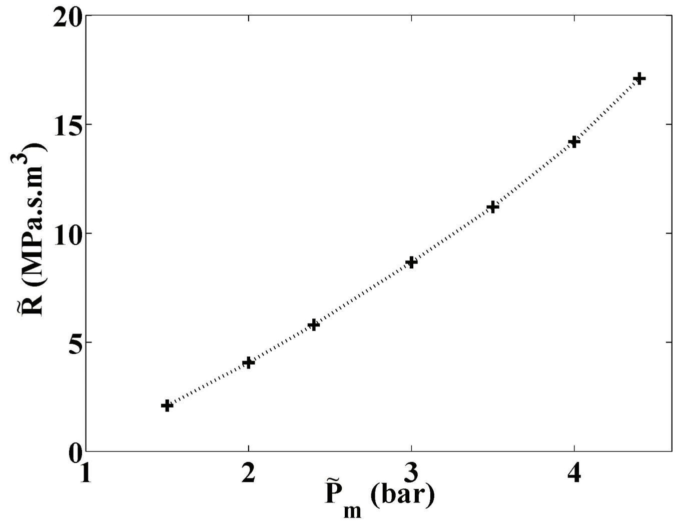

Figure 12: Dimensional load $\tilde{R}$ yielding critical temperatures of Atchley et al.[8], vs. mean pressure $\tilde{P}_m$.

angular frequency corresponds to the first harmonic, since this is the mode that destabilizes first. These values are found to be in qualitative agreement with the above mentioned values $\tilde{R}$ obtained numerically, thus lossless acoustics with a loaded end can adequately model a dissipative resonator. Moreover, the value of the load strongly influences the ability of the thermoacoustic engine to start on its own.

VII. Conclusion

The dynamics of a thermoacoustic engine was investigated numerically for varying mean pressure and temperature ratio between heater and cooler. The model is based upon a low Mach number assumption, leading to a combination between a numerical solution of the flow and heat transfer the active cell and an analytical solution of linear acoustics in the resonator. Numerical simulations were carried out on existing thermoacoustic engine configurations[22;26], showing how a resistive load influences the onset of thermoacoustic oscillations.

The resistive load was varied to encompass a full range of situations from a resonator with closed end to open end, hence values from infinity to zero. To that effect, for a large number of load values, the critical temperature ratio was determined, as well as the angular frequency of the most unstable mode. Results show that for a wide range of intermediate load values, the critical temperature ratio is so high that in practice the engine will not start on its own.

The active cell consisted of a stack of parallel plates placed between heat exchangers also made of plates aligned with the stack plates. For that simple configuration, comparison was possible between the numerical results and a theoretical analysis based on Rott's linear theory. Good agreement was found for both the critical temperature ratio and the dominant oscillation frequency. The hybrid numerical model will be most useful whenever realistic active cell with complex geometry must be dealt with, for example for misaligned plates, or even for fully three-dimensional configurations.

The current model of a lossless resonator associated to a resistance placed at the resonator end can be extended to describe real loads to which the thermoacoustic engine is coupled. The approach used also allowed to account for dissipation in a simple experimental resonator with closed end[8], provided the resistive load value is adequately chosen. In that case, the load is mainly associated to the thermal resistance of the resonator.

Acknowledgements

This work was financed by a PhD grant from Université Pierre et Marie Curie. Support of the Natural Sciences and Engineering Research Council of Canada is gratefully acknowledged (L. B.).

REFERENCES

1. G. W. Swift, "Thermoacoustic engines," J. Acoust. Soc. Am. **84**, 1145–1180 (1988).

2. R. Radebaugh, "A review of pulse tube refrigerators," Adv. Cryog. Eng. **35**, 1191–1205 (1990)

3. A. Migliori and G. W. Swift, "Liquid sodium thermoacoustic engine," Appl. Phys. Lett. **53**, 355–357 (1988).

4. C. Jensen and R. Raspet , “Thermoacoustic power conversion using piezoelectric transducer,” J. Acoust. Soc. Am. **128** (1), 98–103 (2010).

5. N. Rott, “Damped and thermally driven acoustic oscillations in wide and narrow tubes,” Z. Angew. Math. Phys. **20**, 230–243 (1969).

6. W. P. Arnott, H. E. Bass, R. Raspet, “General formulation of thermoacoustics for stacks having arbitrarily shaped pore cross section,” J. Acoust. Soc. Am. **90**, 3228–3237 (1991).

7. B. Ward, J. Clark and G. W. Swift, “Design Environment for Low-Amplitude Thermoacoustic Energy Conversion (DeltaEC) User’s Guide (version 6.2),” Los Alamos National Laboratory (2008).

8. A. A. Atchley and F. M. Kuo, “Stability curves for a thermoacoustic prime mover,” J. Acoust. Soc. Am. **95**, 1401–1404 (1994).

9. W. P. Arnott, J. R. Belcher, R. Raspet, and H. E. Bass, “Stability analysis of a helium-filled thermoacoustic engine,” J. Acoust. Soc. Am. **96**, 370–375 (1994).

10. T. Yazaki, A. Iwata, T. Maekawa and T. Tominaga, “Travelling wave thermoacoustic engine in a looped tubeT,” Phys. Rev. Lett. **81**, 3128–3131 (1998).

11. N. Sugimoto, “Thermoacoustic-wave equations for gas in a channel and a tube subject to temperature gradient,” J. Fluid Mech. **658**, 89–116 (2010).

12. H. Hyodo and N. Sugimoto, “Stability analysis for the onset of thermoacoustic oscillations in a gas-filled looped tube,” J. Fluid Mech. **741**, 585–618 (2014).

13. A. T. A. M. de Waele, “Basic treatement of onset conditions and transient effects in thermoacoustic Stirling engines,” J. Sound Vib. **325**, 974–988 (2009).

14. M. Guedra, G. Penelet, P. Lotton and J.-P. Dalmont, “Theoretical prediction of the onset of thermoacoustic instability from the experimental transfer matrix of a thermoacoustic core,” J. Acoust. Soc. Am. **130**, 145–152 (2011).

15. M. Guedra, G. Penelet, and P. Lotton , “Experimental and theoretical study of the dynamics of self-sustained oscillations in a standing wave thermoacoustic engine,” J. Appl. Phys. **115**, 0245041–0245047 (2014).

16. J. R. Olson and G. W. Swift, “A loaded thermoacoustic engine,” J. Acoust. Soc. Am. **98**, 2690–2693 (1995).

17. R. Bao, G. B. Chen, K. Tang, Z. Z. Jia, W. H. Cao, “Effect of RC load on performance of thermoacoustic engine,” Cryogenics **46**, 666–671 (2006).

18. P. Duthil, D. Baltean Carlès, A. Bétrancourt, M.-X. François., Z. B. Yu, J. P. Thermeau, “Experiments and valve modeling in thermoacoustic device,” Adv. Cryog. Eng. **51**(B),1095–1102 (2006).

19. H. Hatori, T. Biwa, T. Yazaki, “How to build a loaded thermoacoustic engine,” J. Appl. Phys. **111**, 074905 (2012).

20. G. Y. Yu, E.C. Luo, W. Dai, J. Y. Hu, “Study of nonlinear processes of a large experimental thermoacoustic-Stirling heat engine by using computational fluid dynamics,” J. Appl. Phys. **102**, 074901–074907 (2007).

21. J. A. Lycklama à Nijeholt, M. E. H. Tijani, S. Spoelstra, “Simulation of a traveling-wave thermoacoustic engine using Computational Fluid Dynamics,” J. Acoust. Soc. Am. **118**, 2265–2270 (2005).

22. O. Hireche, C. Weisman, D. Baltean-Carlès, P. Le Quéré, L. Bauwens “Low Mach number analysis of idealized thermoacoustic engines with numerical solution,” J. Acoust. Soc. Am. **128** (6), 3438–3448 (2010)

23. R. Raspet, J. Bruster, H. E. Bass "New Approximation Method for Thermoacoustic Calculations," J. Acoust. Soc. Am. **103** (5), 2395–2402 (1998)

24. N. Rott, "Thermoacoustics," Adv. Appl. Mech. **20**, 135-243 (1980).

25. G. W. Swift, *A unifying perspective for some engines and refrigerators* (ASA, Melville, USA, 2002), eq. 4.70 on p. 90.

26. A. A. Atchley, H. E. Bass, T. J. Hofler, H. T. Lin, "Study of a thermoacoustic prime mover below onset of self-oscillation," J. Acoust. Soc. Am. **91**, 734–743 (1992).

Table 1: Dimensionless parameters characterizing the reference experimental device[22]

M	P_e	P_{es}	R_e	$\hat{l}_L$	H	h/H	h_x/H	L_{hx}	L_{cx}	L_{xs}
0.02	1100	4900	1600	0.09	0.007	0.73	0.73	0.05	0.05	0.005

Table 2: Fluid properties in reference experiment[22]

Helium gas					
$\tilde{P}_m$	$\tilde{T}_c$	$\tilde{\rho}$	$\tilde{\mu}$	$\tilde{c}_p$	$\tilde{k}$
MPa	K	$kg \cdot m^{-3}$	$Pa \cdot s$	$J \cdot kg^{-1} K^{-1}$	$W \cdot m^{-1} K^{-1}$
1.0	293	1.6	2.10^{-5}	5193	0.15

Figure Captions

Figure 1. Simplified geometry of a thermoacoustic engine.

Figure 2. Geometry of resonator (a) and of active cell geometry (b) in dimensionless coordinates.

Figure 3. (a) Typical time signal of acoustic pressure $p'(0,t)$, and (b) (color online) associated spectrogram (the magnitude is the square root of the power density spectrum). $Z = 0.988$. $T_h = 1.08$.

Figure 4. Growth rate of most unstable mode as a function of the hot exchanger temperature, $Z = -0.963$.

Figure 5. Stability diagram in the (Z, T_h) plane, showing the stability curve -●-. The region above the curve corresponds to instability.

Figure 6. Angular frequency of the most unstable mode scaled by ω_{ref}, as a function of Z.

Figure 7. Growth rates as a function of the active cell location for $0 < \hat{l}_L < 0.5$, $Z = -0.963$, $T_h = 1.2$. -●- fundamental mode (the $\lambda/2$ mode), -∗- first harmonic mode (the λ mode).

Figure 8. Stability diagram showing the critical temperature ratio as a function of the active cell location for (a) -□- $Z = -0.99$, -∗- $Z = -0.92$, -●- $Z = -0.85$, the critical mode is the fundamental mode ($\lambda/2$), and (b) -●- $Z = 0.79$, -∗- $Z = 0.90$, -□- $Z = 0.99$, the critical mode is the first harmonic ($3\lambda/4$).

Figure 9. Stability diagram in the (Z, T_h) plane, showing the stability curve (critical temperature ratios) for three distances between heat-exchangers and stack, -□- $L_{xs} = 0$,-●- $L_{xs} = h$, -∗- $L_{xs} = 2h$. (a) $-1 < Z < -0.6$, (b) $0.6 < Z < 1$.

Figure 10. Stability diagrams in the (Z, T_h) plane, showing critical temperature ratios, ● Numerical simulation, – – – Linear theory. (a) $-1 < Z < -0.6$; (b) $0.6 < Z < 1$.

Figure 11. Frequency of the most unstable modes vs. Z. □ linear theory, × simulations, (a) $-1 < Z < -0.6$; —— resonant frequencies of a closed-closed lossless resonator with

temperature discontinuity at $\hat{x} = 0$ and $T_h = T_{crit}(Z)$ determined by numerical simulations, $- - -$ approximate vertical separation between modes (multiples of $\lambda/2$), (b) $0.6 < Z < 1$, —— resonant frequencies of an open-closed lossless resonator with temperature discontinuity at $\hat{x} = 0$ and $T_h = T_{crit}(Z)$, $- - -$ approximate vertical separation between modes (odd multiples of $\lambda/4$).

Figure 12. Dimensional load $\tilde{R}$ yielding critical temperatures of Atchley et al.[8], vs. mean pressure $\tilde{P}_m$.

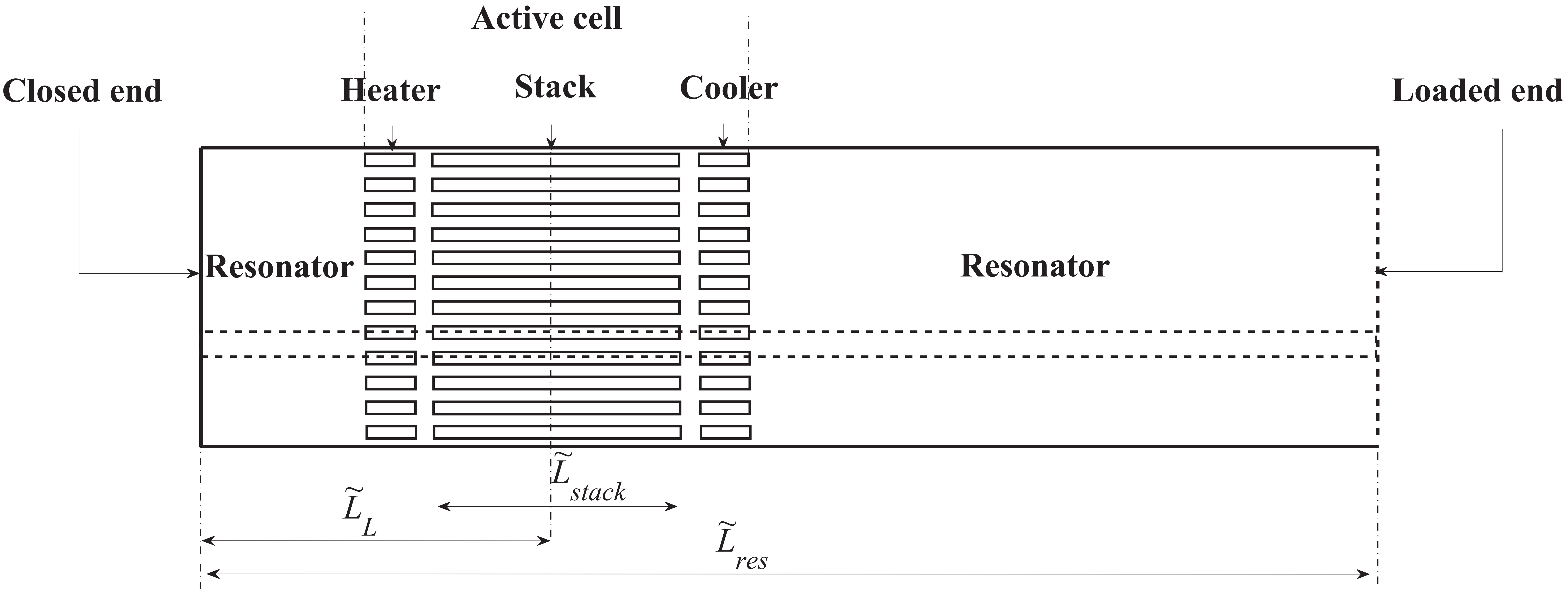
Active cell
Closed end
Heater
Stack
Cooler
Loaded end
Resonator
Resonator
$\widetilde{L}_{stack}$
$\widetilde{L}_L$
$\widetilde{L}_{res}$

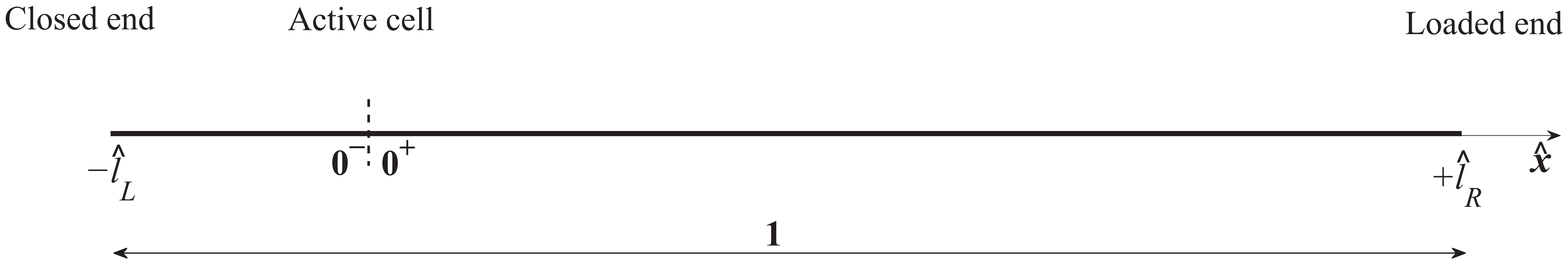
Closed end
Active cell
Loaded end
0^-
0^+
$-\hat{l}_L$
$+\hat{l}_R$
$\hat{x}$
1

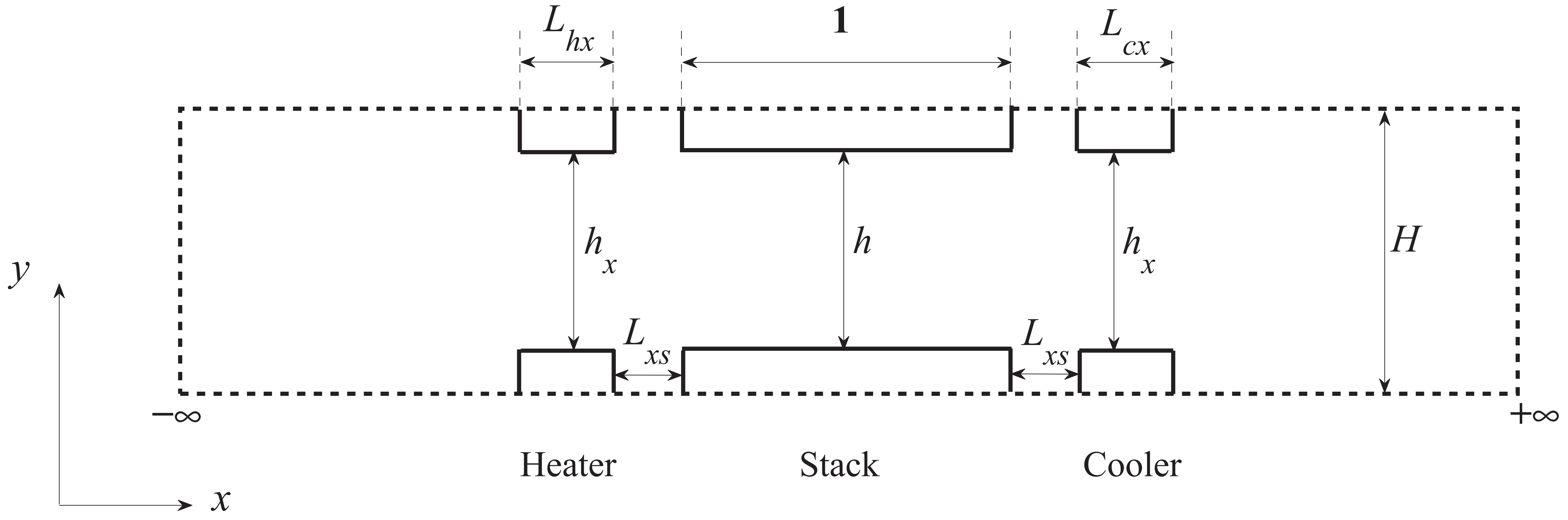

L_{hx}
1
L_{cx}
h_x
h
h_x
H
y
L_{xs}
L_{xs}
$-\infty$
$+\infty$
Heater
Stack
Cooler
x

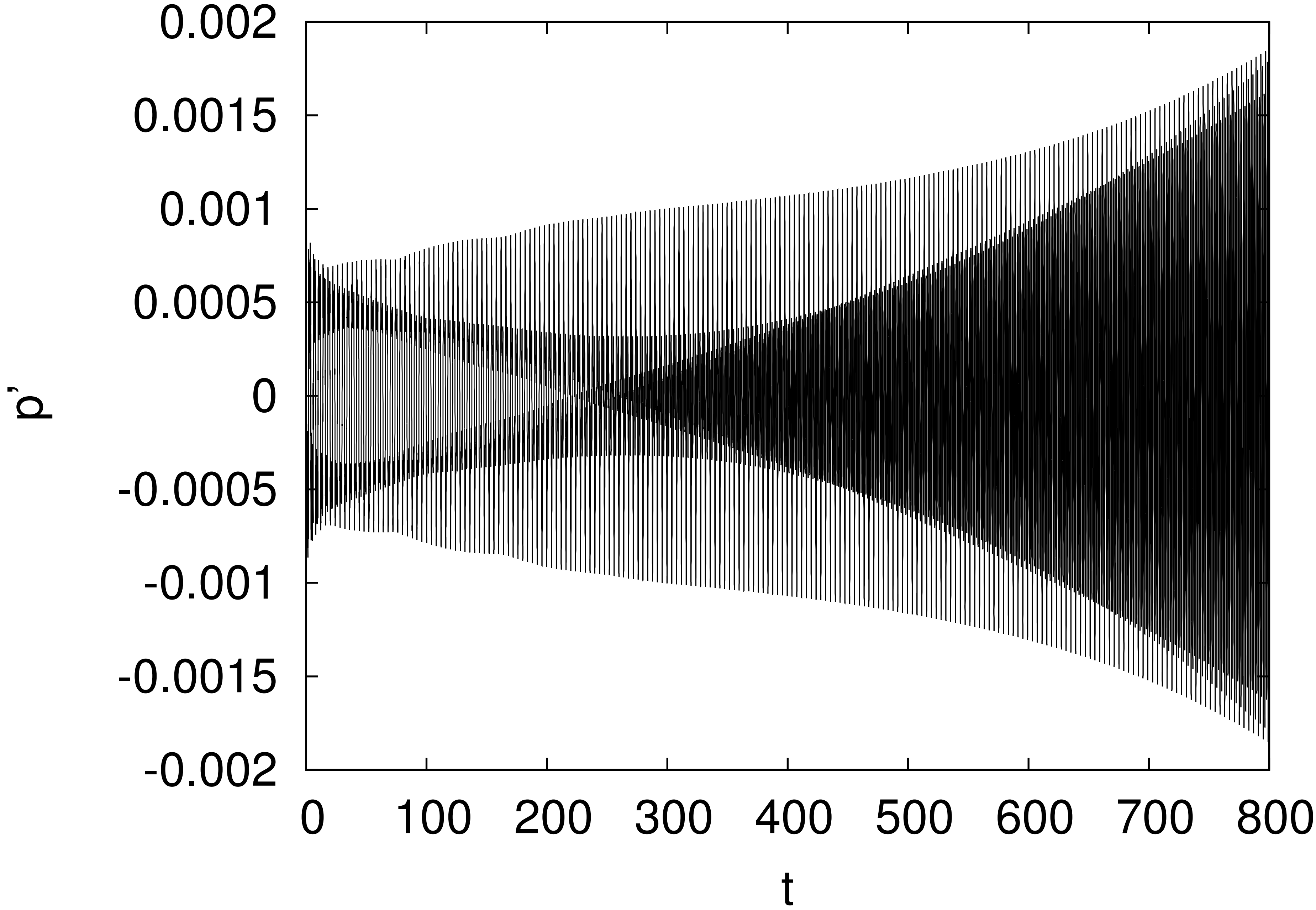
0.002
0.0015
0.001
0.0005
0
-0.0005
-0.001
-0.0015
-0.002
p'
0
100
200
300
400
500
600
700
800
t

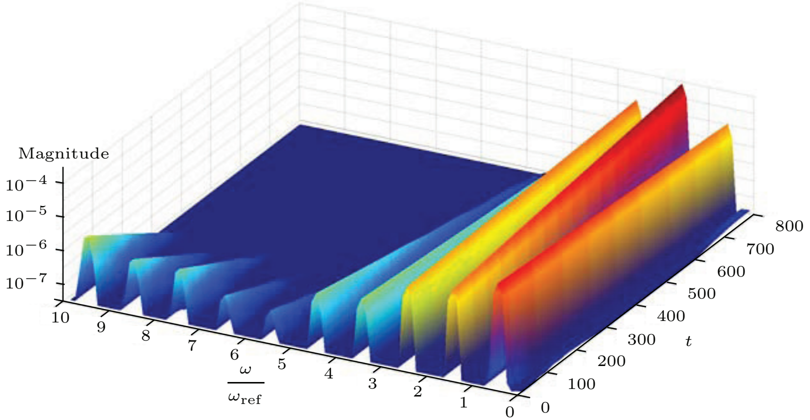
Magnitude
10^{-4}
10^{-5}
10^{-6}
10^{-7}
10
9
8
7
6
5
4
3
2
1
0
$\frac{\omega}{\omega_{\mathrm{ref}}}$
0
100
200
300
400
500
600
700
800
t

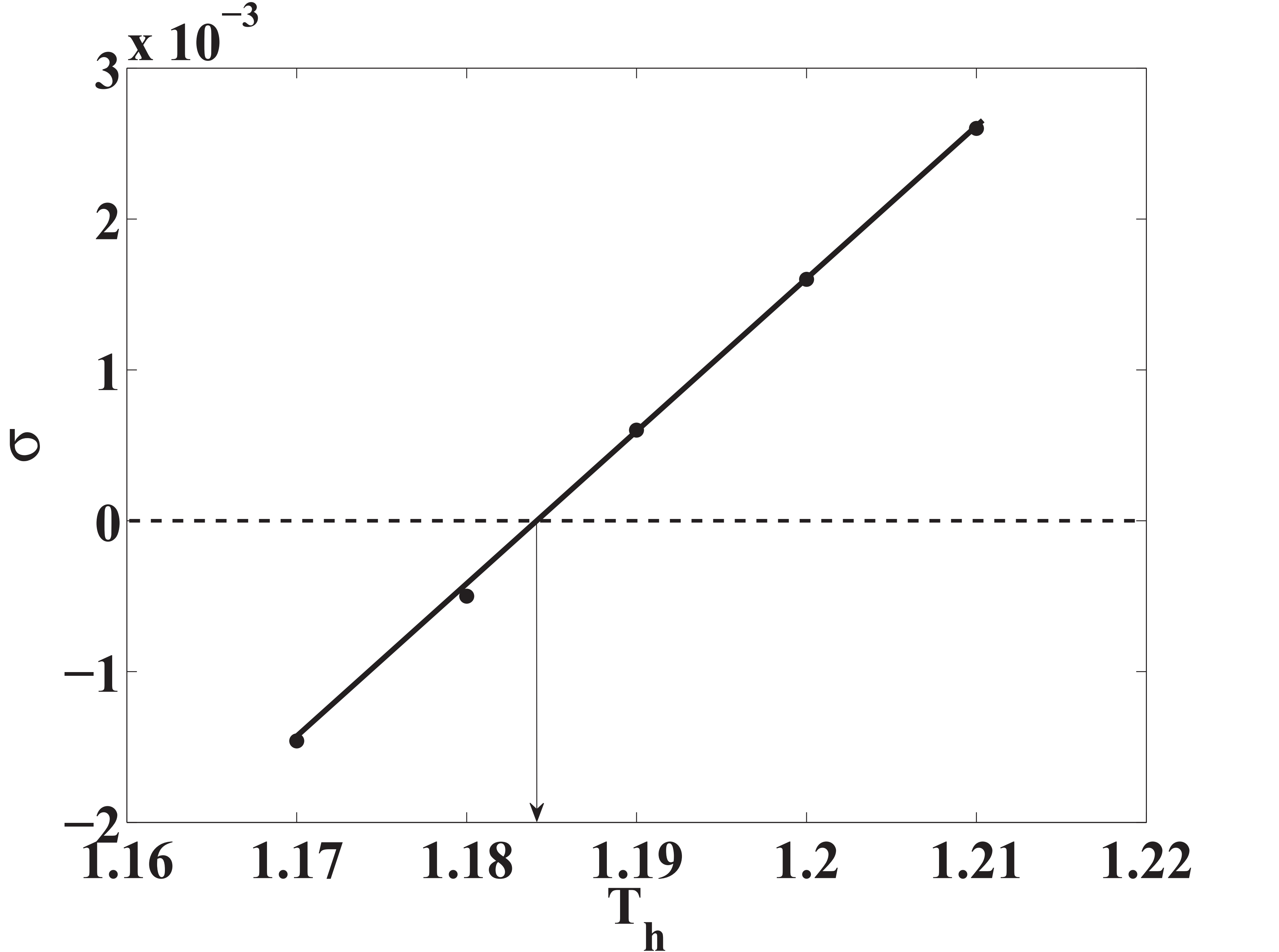
x 10^−3
3
2
1
0
−1
−2
σ
1.16
1.17
1.18
1.19
1.2
1.21
1.22
T_h

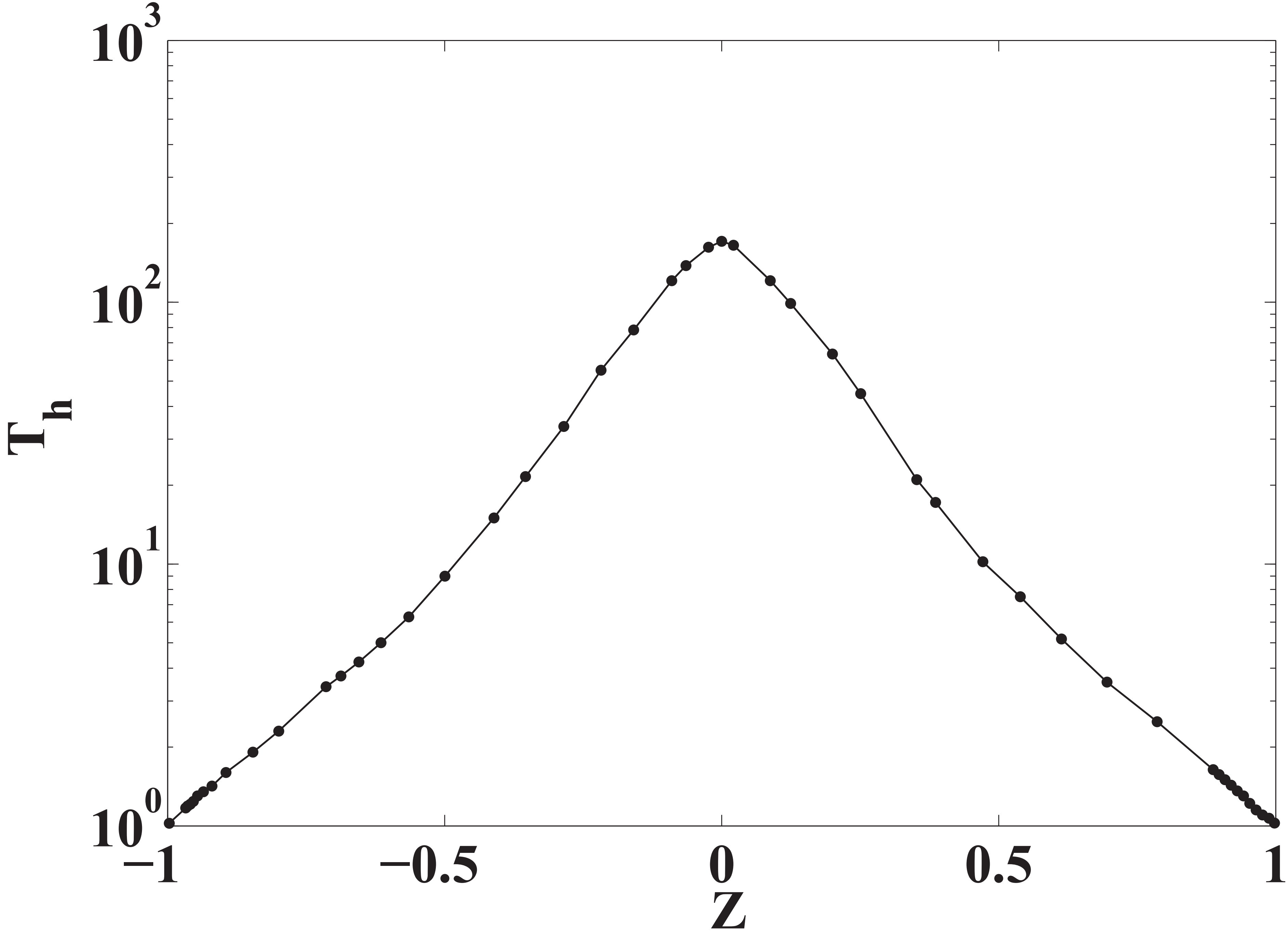

10^3
10^2
10^1
10^0
T_h
−1
−0.5
0
0.5
1
Z

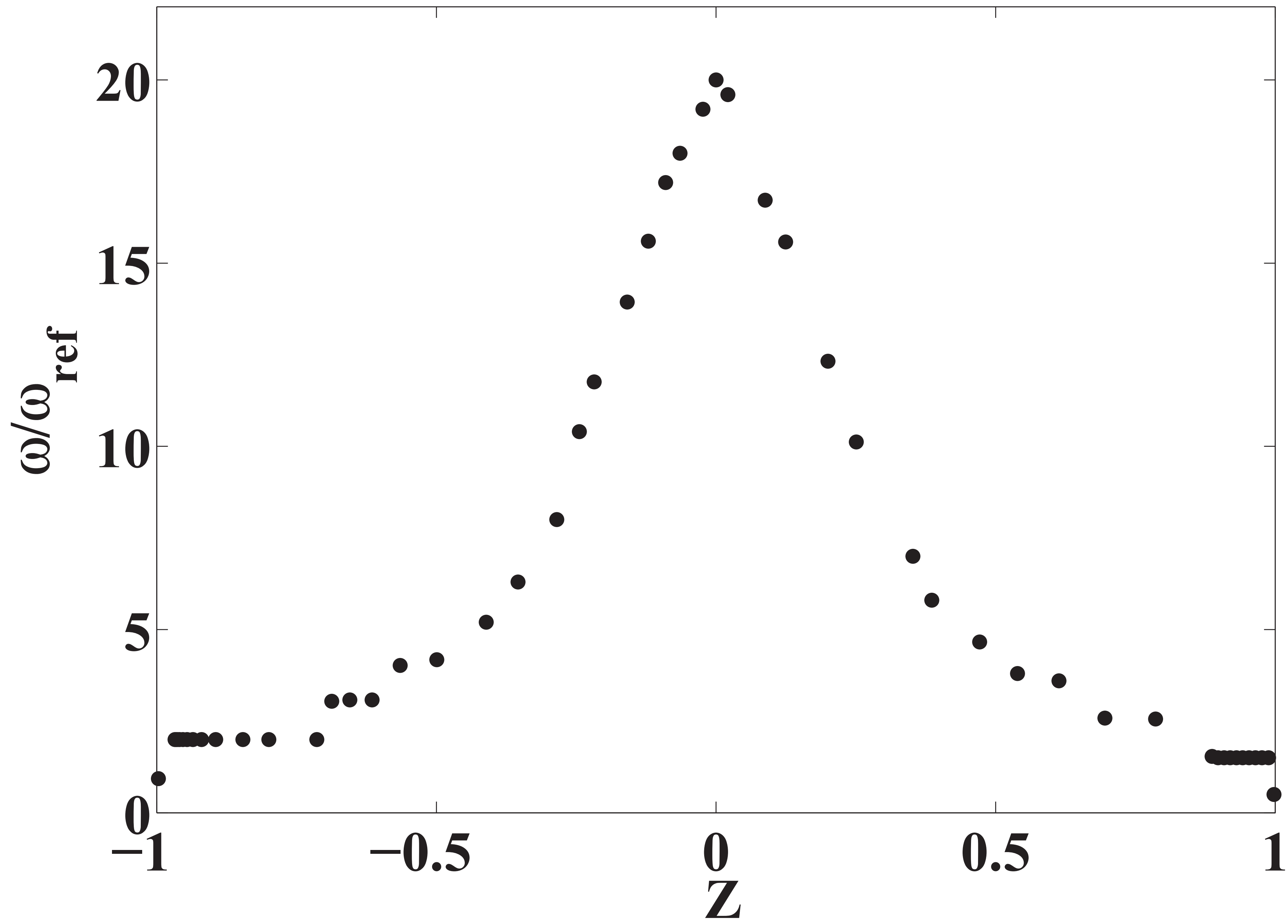

20
15
10
5
0
−1
−0.5
0
0.5
1
Z
ω/ω_ref

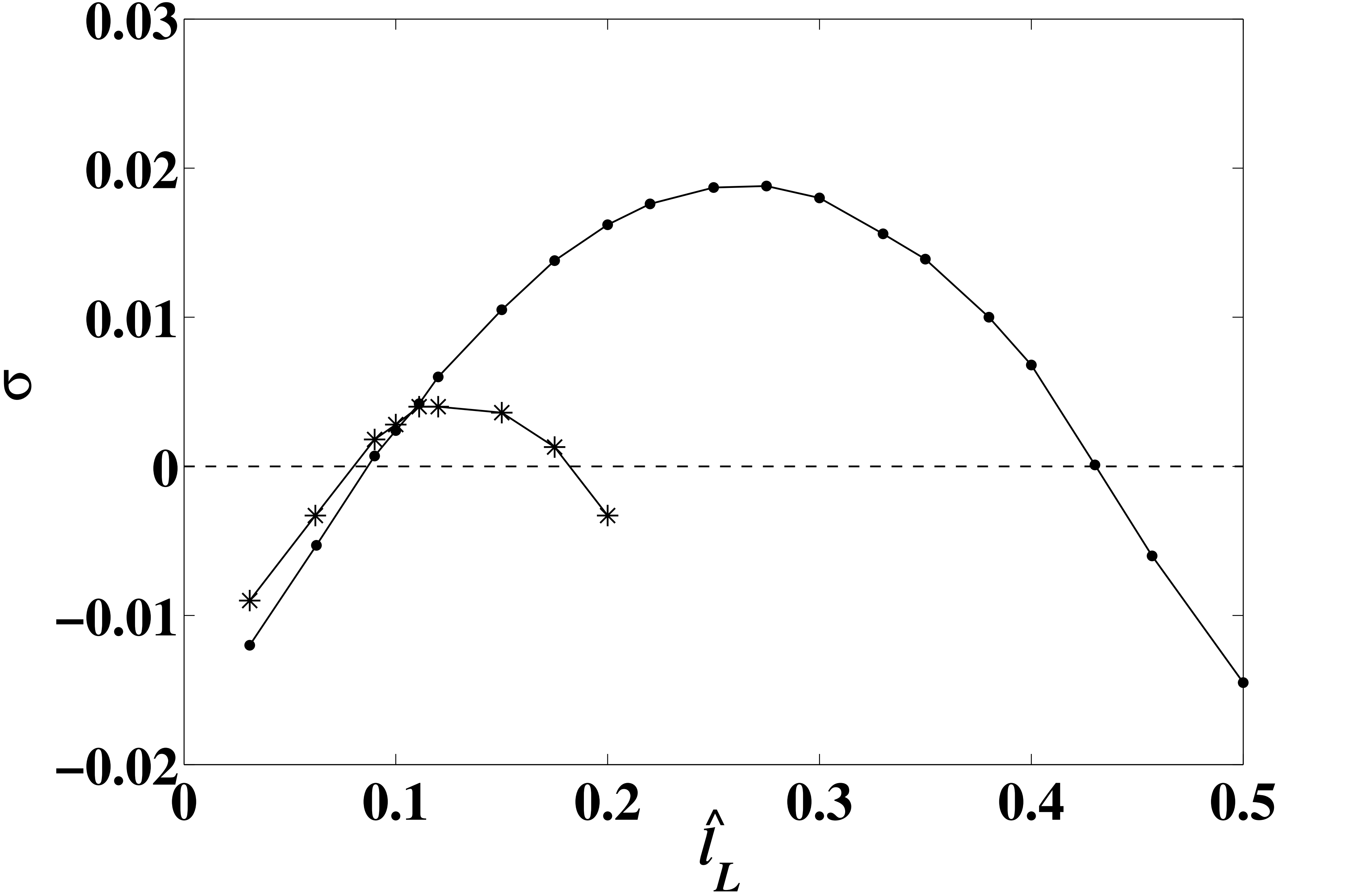
0.03
0.02
0.01
0
−0.01
−0.02
σ
0
0.1
0.2
0.3
0.4
0.5
$\hat{l}_L$

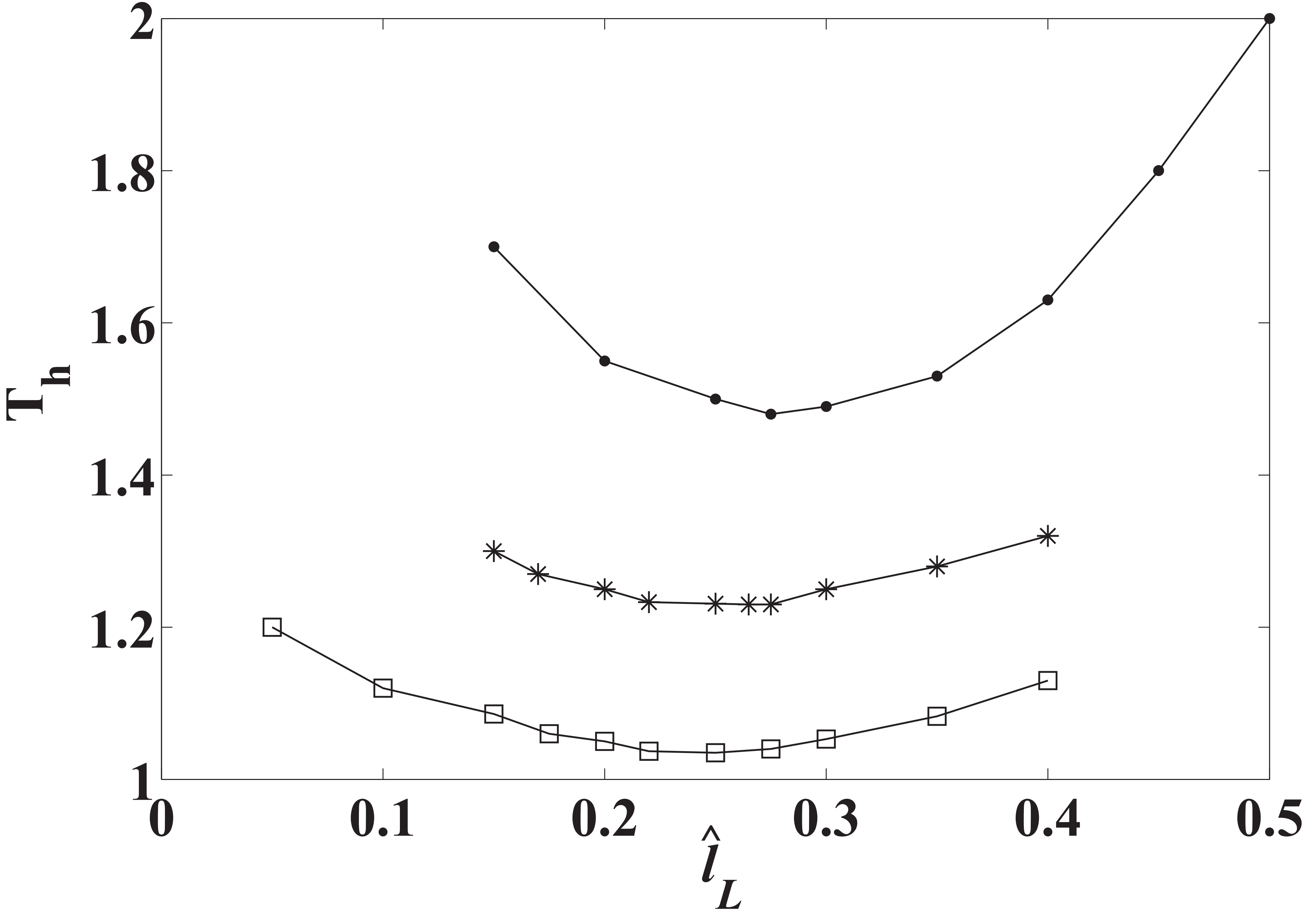

2
1.8
1.6
1.4
1.2
1
T_h
0
0.1
0.2
0.3
0.4
0.5
$\hat{l}_L$

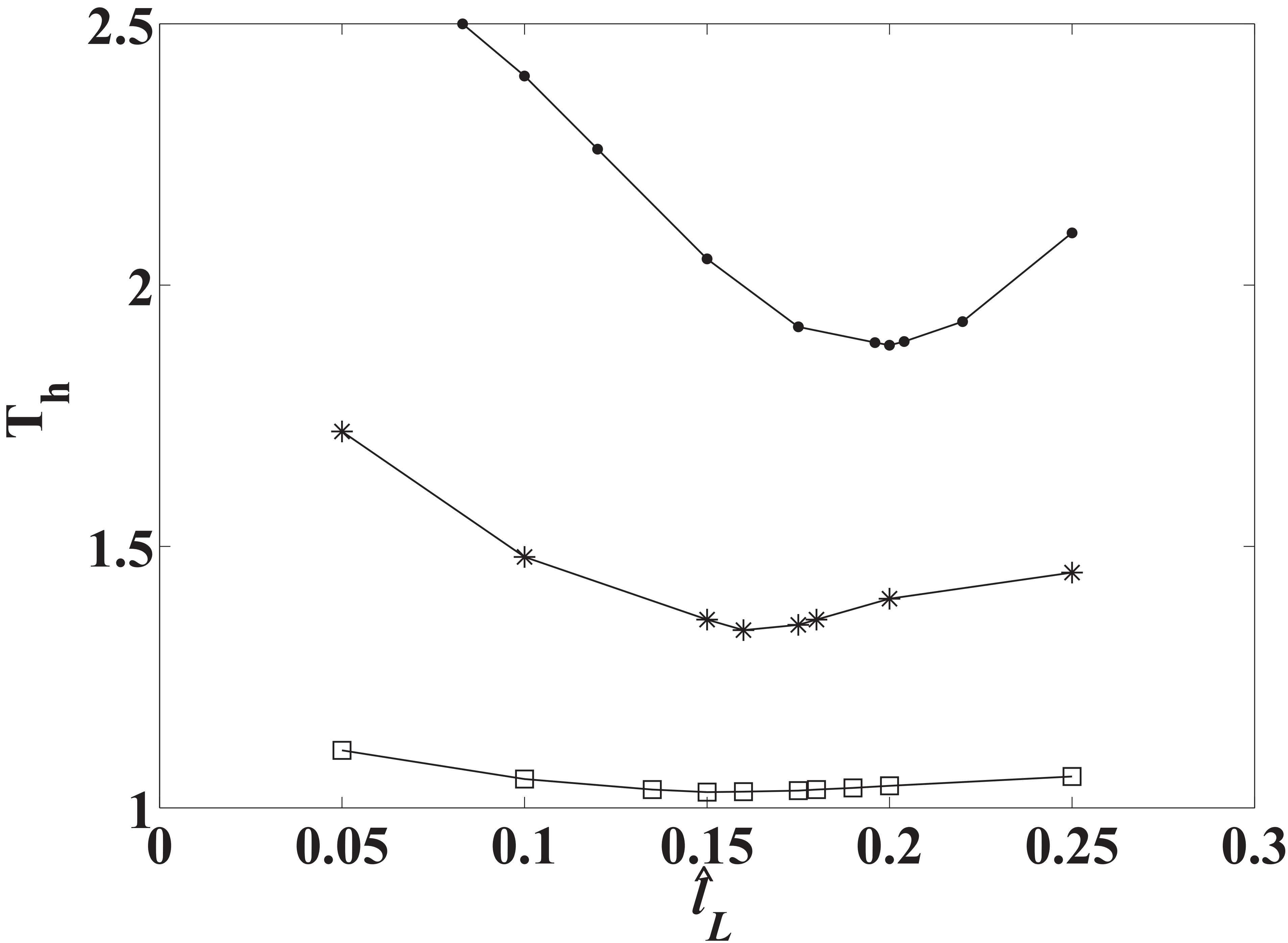
2.5
2
1.5
1
0
0.05
0.1
0.15
0.2
0.25
0.3
T_h
$\hat{l}_L$

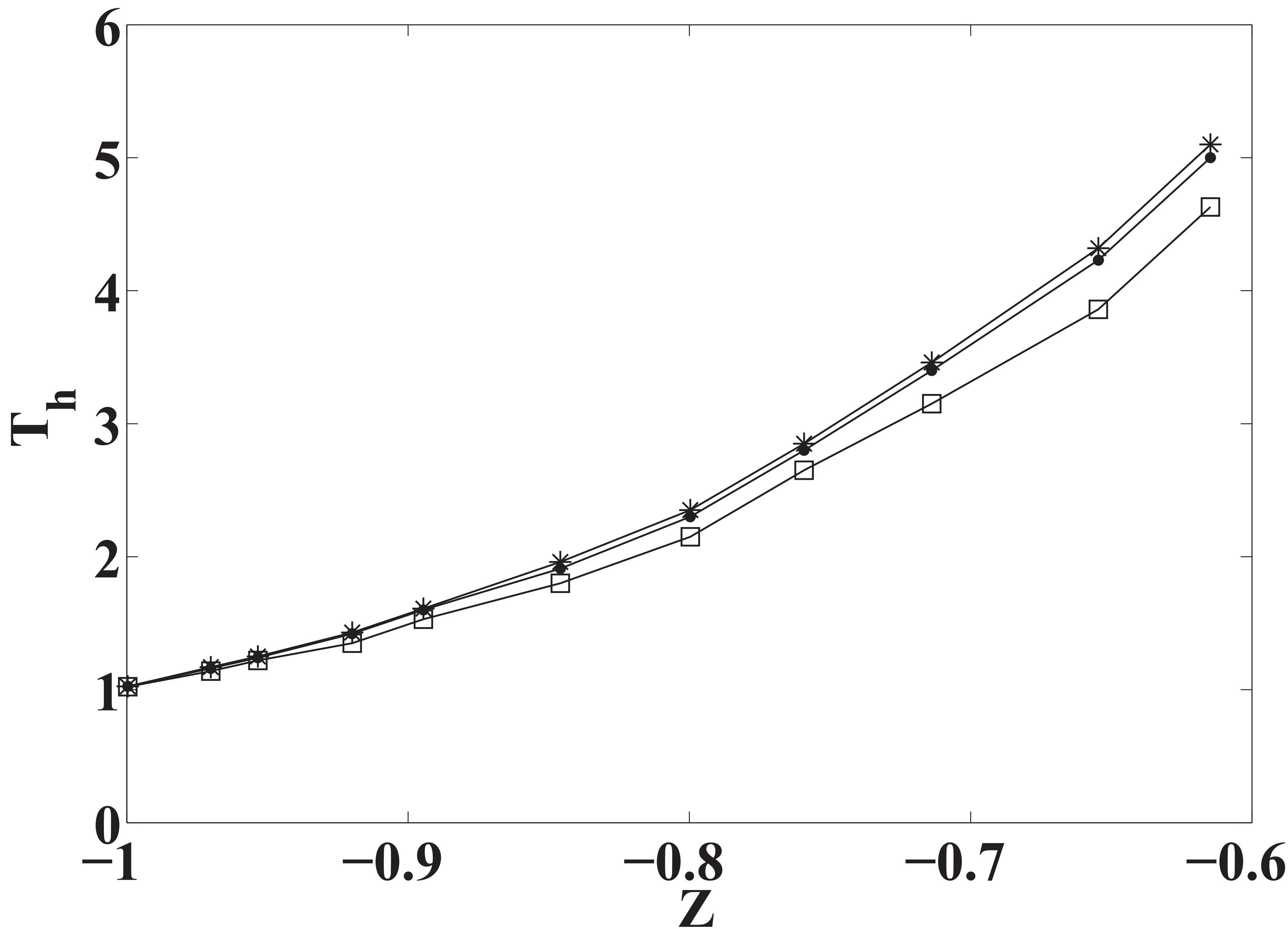

0
1
2
3
4
5
6
T_h
−1
−0.9
−0.8
−0.7
−0.6
Z

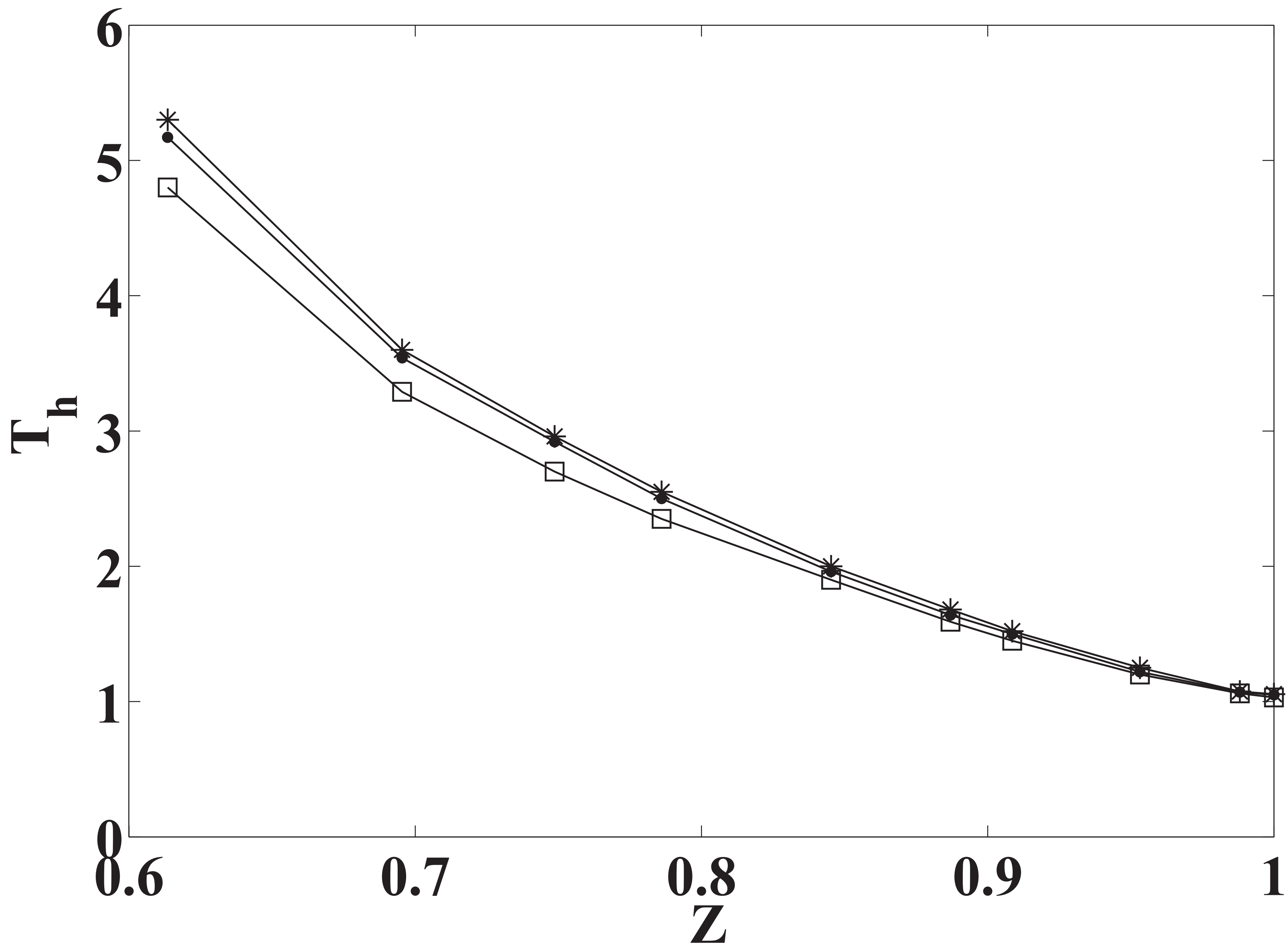

T_h
Z
0
1
2
3
4
5
6
0.6
0.7
0.8
0.9
1

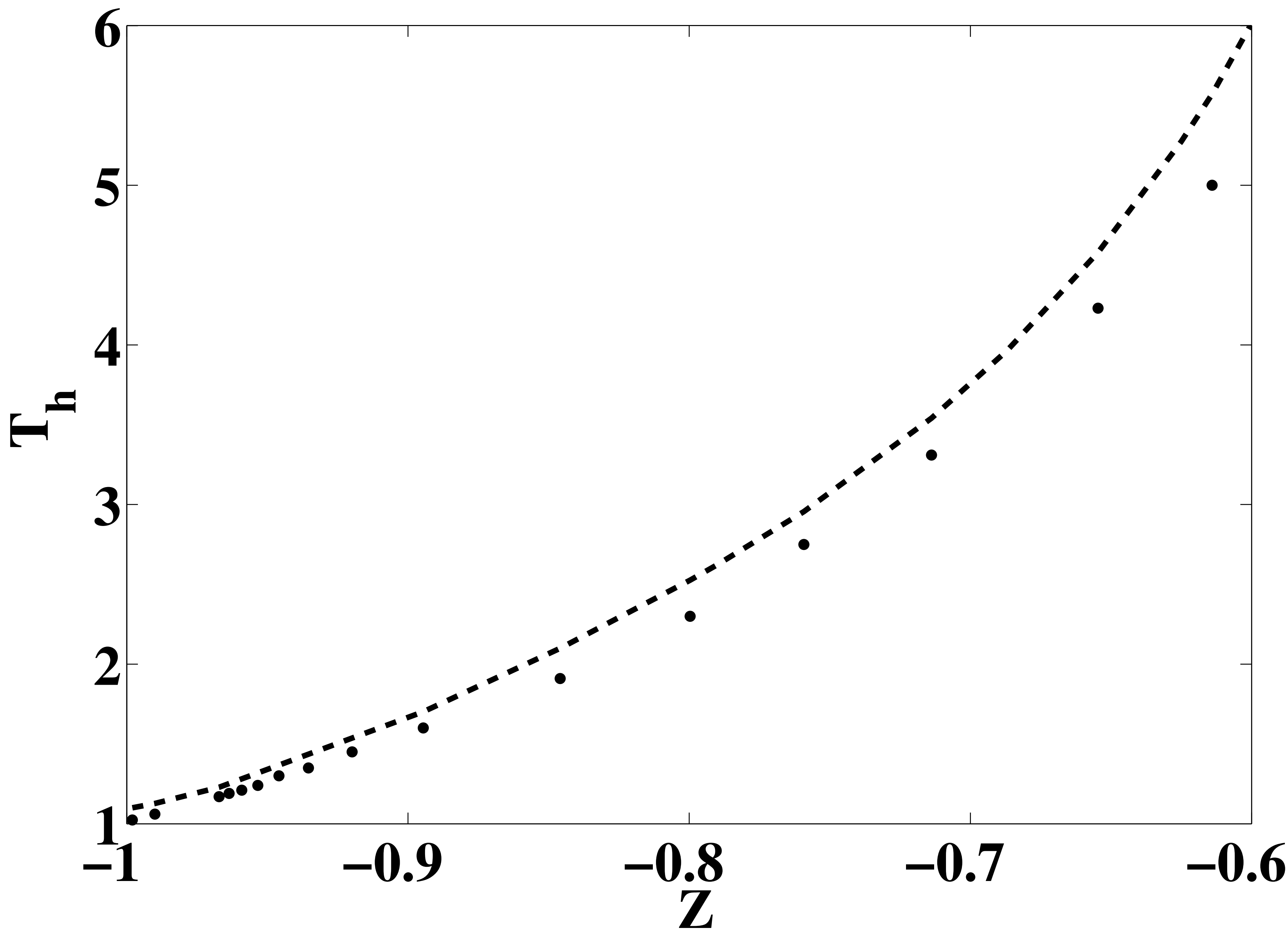

6
5
4
3
2
1
T_h
−1
−0.9
−0.8
−0.7
−0.6
Z

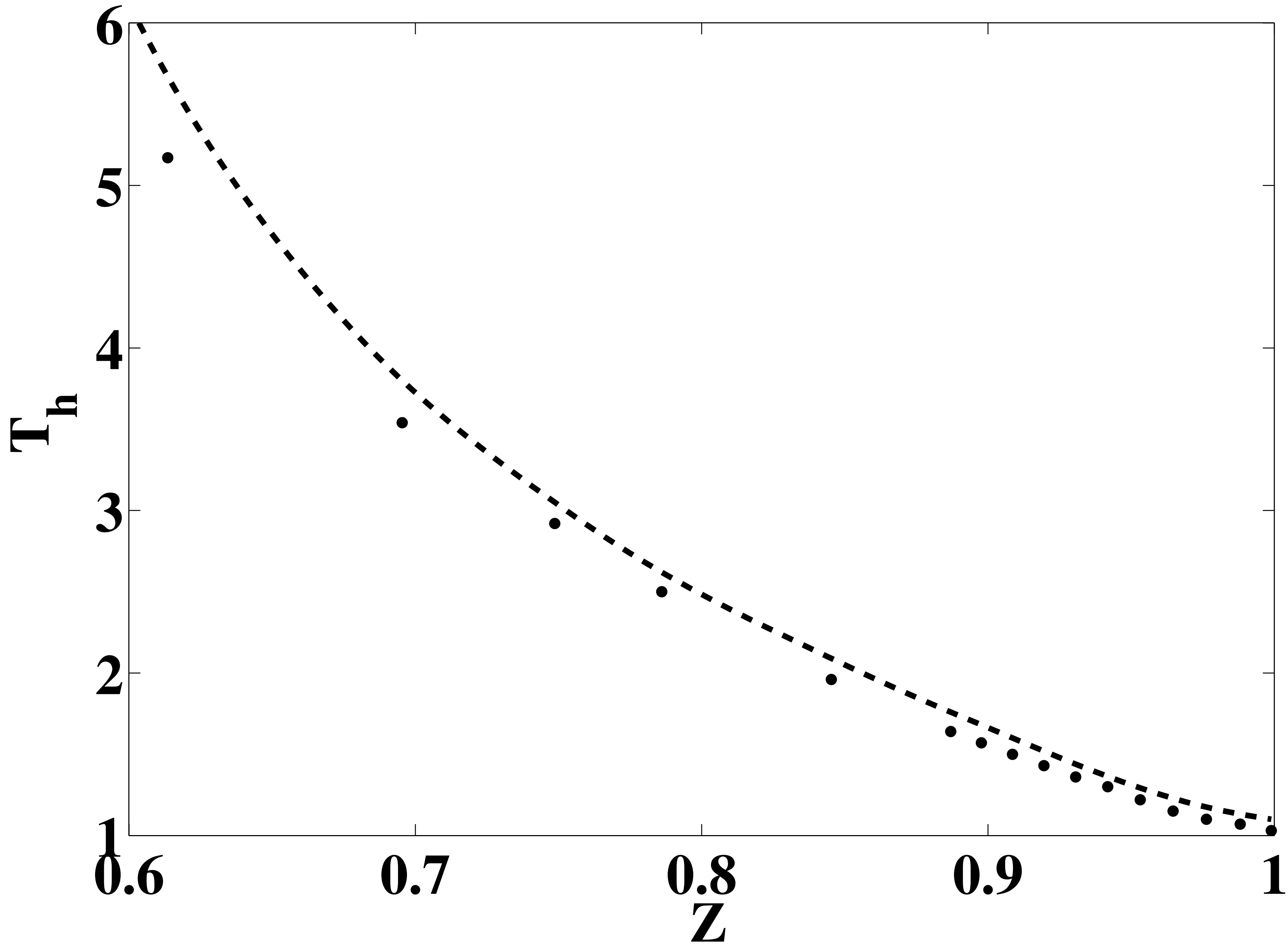

6
5
4
3
2
1
T_h
0.6
0.7
0.8
0.9
1
Z

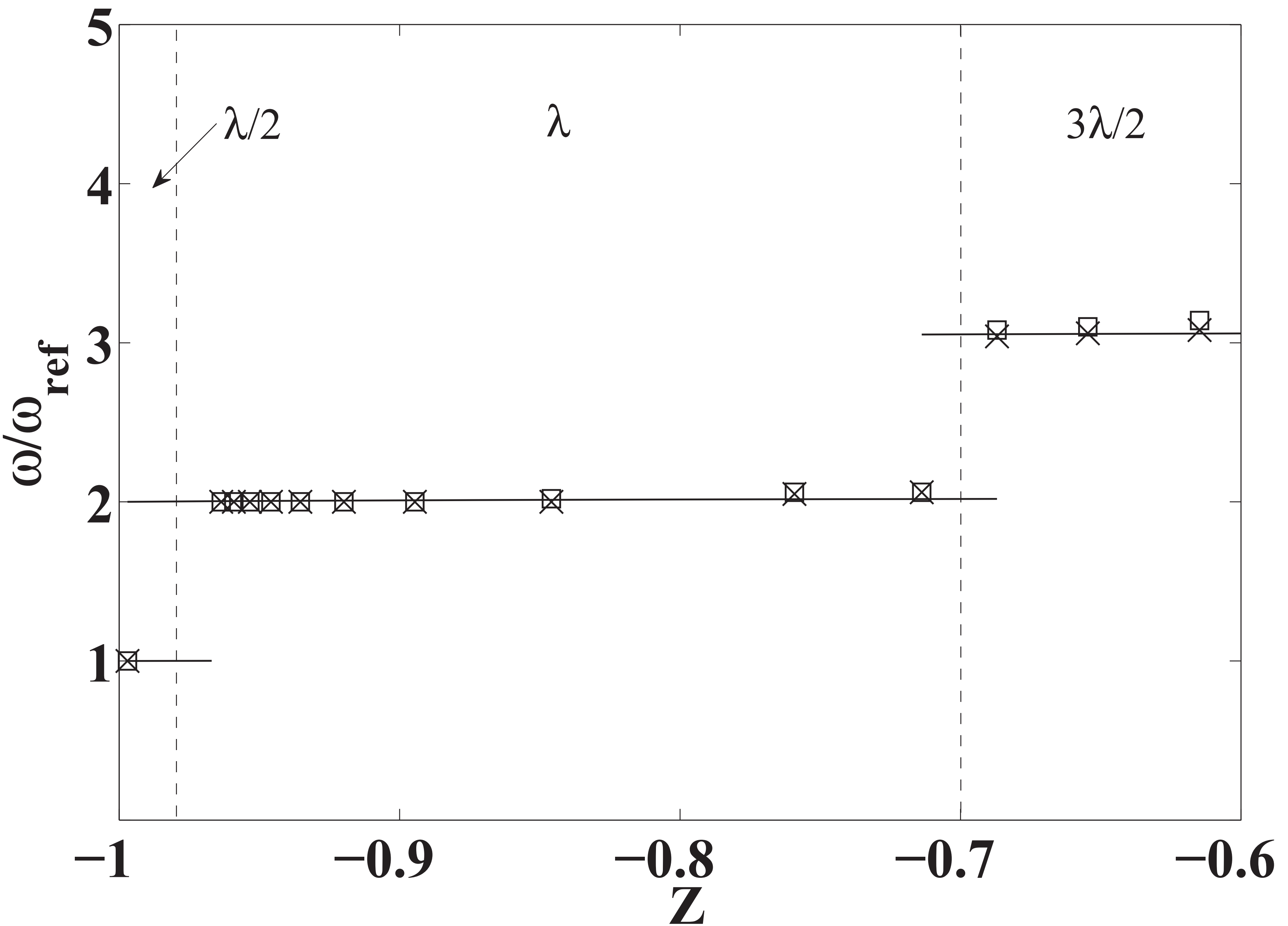

5
4
3
2
1
λ/2
λ
3λ/2
ω/ω_ref
−1
−0.9
−0.8
−0.7
−0.6
Z

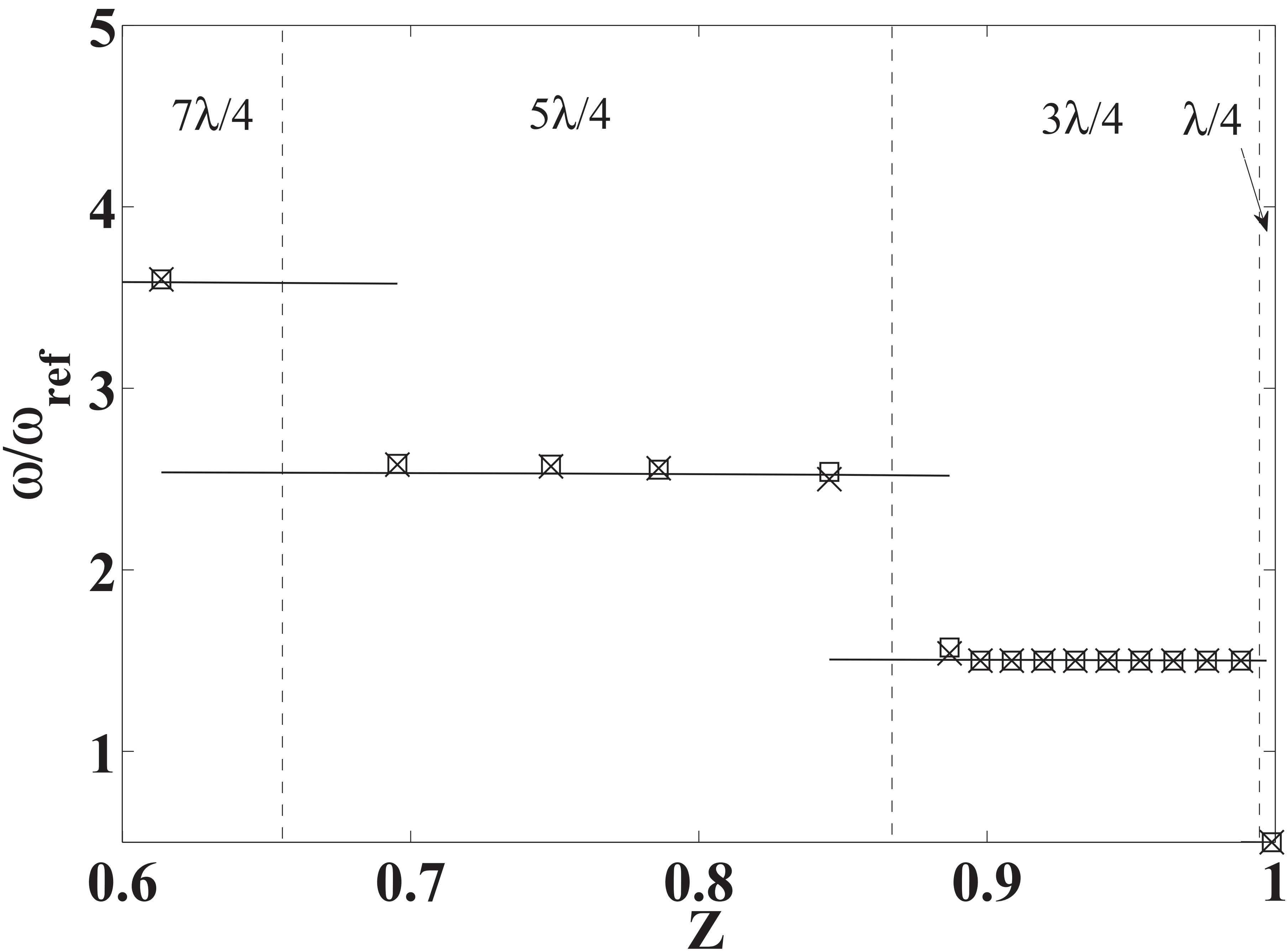

5
4
3
2
1
ω/ω_{ref}
$7\lambda/4$
$5\lambda/4$
$3\lambda/4$
$\lambda/4$
0.6
0.7
0.8
0.9
1
Z

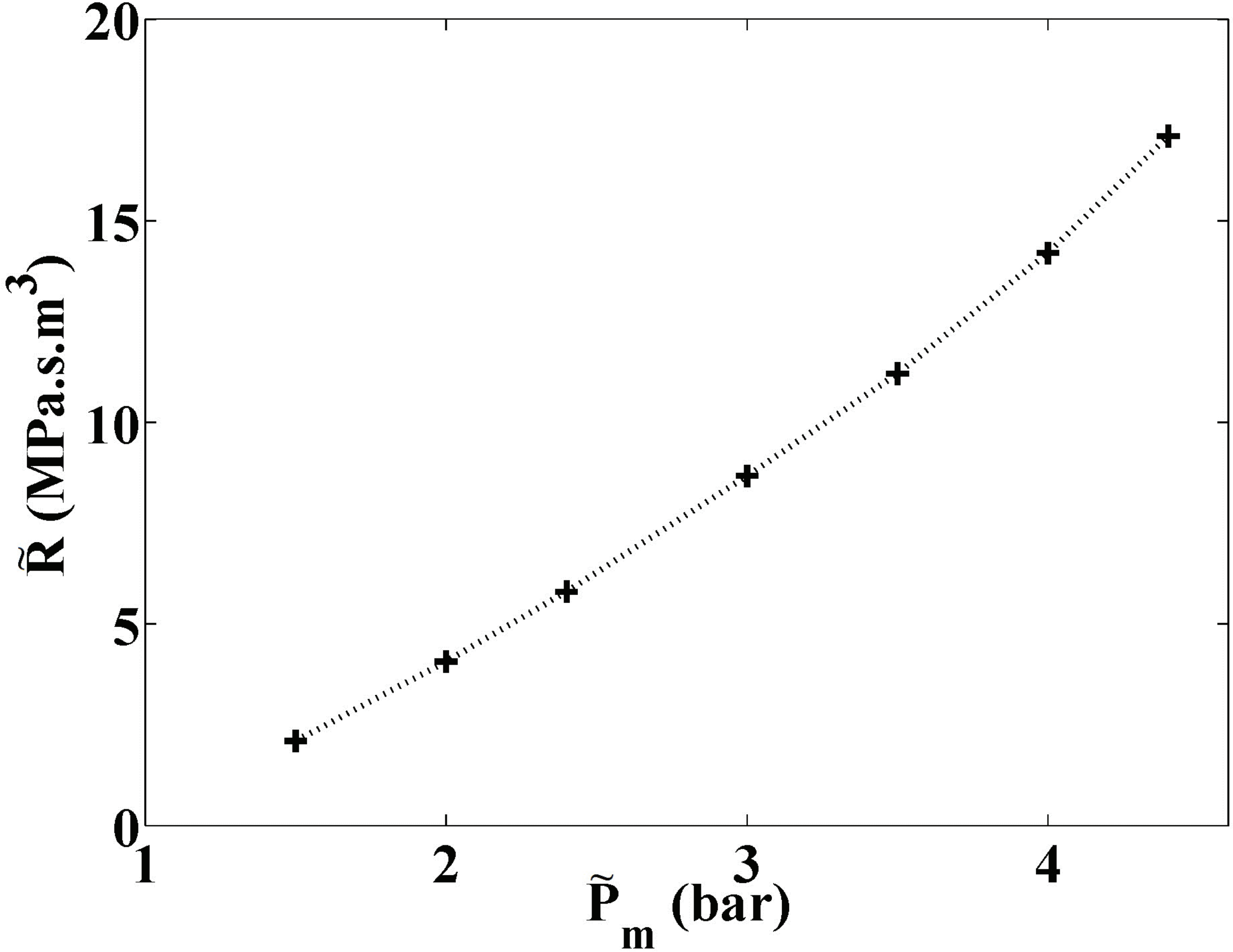
20
15
10
5
0
1
2
3
4
$\tilde{R}$ (MPa.s.m^3)
$\tilde{P}_m$ (bar)